CHALMERS

Large Eddy Simulation of flow around a Gas Turbine Outlet Guide Vane

Master's Thesis in Fluid Dynamics

ANSUMAN PRADHAN

Department of Applied Mechanics
Division of Fluid Dynamics
Chalmers University of Technology
Göteborg, Sweden, 2014
Master's Thesis 2014:79

MASTER'S THESIS 2014:79

Large Eddy Simulation of flow around a Gas Turbine Outlet Guide Vane

Ansuman Pradhan

Department of Applied Mechanics
Division of Fluid Dynamics
CHALMERS UNIVERSITY OF TECHNOLOGY
Göteborg, Sweden, 2014

Large Eddy Simulation of flow around a Gas Turbine Outlet Guide Vane
Master's Thesis in Fluid Dynamics

Master's Thesis 2014:79
ISSN: 1652-8557

Department of Applied Mechanics
Division of Fluid Dynamics
Chalmers University of Technology
SE-41296, Göteborg
Sweden
Tel. +46 (0)31-772 1000

Reproservice / Department of Applied Mechanics
Göteborg, Sweden 2014

Abstract

Engineering flows in the practical world are chaotic and comprise of many different scales of motion due to the influence of ambient noise or disturbances. Such disturbances have a significant impact on the nature of flow close to the boundaries/walls. To simulate such flows near the boundaries correctly constitutes an important aspect of designing and product development processes. In the present thesis flow around a low-pressure turbine outlet guide vane (LPT-OGV) is studied using Large Eddy Simulations (LES). Effort is made to capture the boundary layer transition over the guide vane, which has a crucial impact on the heat transfer characteristics at the vane walls. The results are compared with experimental studies performed on the OGV at the department. Previous simulations based on this experimental study was performed via RANS (Reynolds averaged Navier Stokes) modelling approach. It is the first time that LES is being used. A finite volume method based in-house solver in Fortran, called CALC-LES, is used for performing simulations. The computational grid is created using another in-house meshing utility, called G3DMESH. The solver of CALC-LES uses a geometric multigrid algorithm to solve the pressure (poisson) equation. In the present thesis, this implementation is studied thoroughly and modifications are made to render it operable for boundary conditions similar to that of the present problem. Two different subgrid scale (SGS) models are used for performing comparative studies – the Smagorinsky-Lilly model and the Germano-Lilly dynamic model. The present simulations fail to capture the transition in the boundary layer over the OGV. The pressure distribution corroborates with the experimental data; but the same cannot be said for the heat transfer at the walls. Mesh independence study showed that the spanwise resolution and domain width of the mesh hardly played any role in transition. Better result from a mesh with finer streamwise resolution in the transition zone indicated that probably a finer streamwise mesh throughout the surface is required for transition prediction. Studying the resolved Reynolds stress components in the boundary layer revealed that the streamwise stress component increased in magnitude significantly, but it doesn't get distributed into the other components. As a result transition is not observed. Further inspection of the turbulent kinetic energy peak showed that probably the streamwise streaks grow, but either they were not big enough to trigger transiiton or there was no continuous forcing provided by the free-stream turbulence to trigger transition.

Keywords: CFD, LES, boundary layer transition, bypass, FST, heat transfer, multigrid method, guide vane.

Acknowledgements

To start with, first I would like to express my deepest gratitude towards my supervisor, Prof. Lars Davidson, for sharing some of his profound knowledge in turbulence modelling with me. Throughout the thesis, he has been extremely patient with me, which has allowed me to learn things at my own pace. I would also like to thank Asst. Prof. Niklas Andersson, for helping me in understanding the script for mesh-generation.

I would like to acknowledge my colleagues, Manan and Sankar, for all the discussions we had on various subjects, be it fluid dynamics or mathematics or other abstract topics. It was always enjoyable and insightful. I am also thankful to Himanshu for providing his valuable critique on my thesis report. I also wish to thank *Svenska Institutet*. Without their financial support over the two years of master studies, this thesis wouldn't have been possible.

Finally, I would like to express my gratitude towards my family back home, whose constant support and love helped me in succeeding.

Göteborg,
2014/12/15

Ansuman Pradhan

Nomenclature

Abbreviations

DNS	Direct Numerical Solution
FAS	Full Approximation Storage
FMG	Full Multi-grid
FST	Free-stream Turbulence
GMG	Geometric Multi-grid
GS	Gauss-Seidel
HPT	High Pressure Turbine
LES	Large Eddy Simulations
LKE	Laminar Kinetic Energy
LPT	Low Pressure Turbine
MG	Multi-grid
NS	Navier-Stokes
OGV	Outlet Guide-vane
PPE	Pressure Poisson Equation
RANS	Reynolds-averaged Navier-Stokes equations
rms	Root mean square
SGS	Sub-grid scale
TDMA	Tridiagonal matrix algorithm

TKE Turbulent Kinetic Energy

Greek Symbols

α Thermal diffusivity,$[\nu/Pr]$

α_r Residual/SGS thermal eddy-diffusivity

$\bar{\Delta}$ Grid filter-width

δ_{ij} Kronecker-delta

κ von Kármán constant

ν Kinematic viscosity

ν_r Residual/SGS eddy-viscosity

ρ Density

$\tau_{\theta j}$ Residual/SGS heat flux

τ_{ij}^r Residual/SGS stress tensor

θ Temperature

θ_{in} Inlet Temperature

$\widetilde{\bar{\Delta}}$ Test filter-width

Roman Symbols

C_s Smagorinsky coefficient

l_{smg} Smagorinsky lengthscale

C_p Coefficient of pressure

c_p Heat capacity at constant pressure

c_x Axial chord

I Turbulent Intensity

l_p Pitch of the cascade

l_s Turbulent length scale

p Pressure

Pr Molecular Prandtl Number

Pr_t Turbulent Prandtl number

q	Heat flux rate
S_{ij}	Strain-rate tensor, $\left[\frac{1}{2}\left(\frac{\partial v_i}{\partial x_j}+\frac{\partial v_j}{\partial x_i}\right)\right]$
U_0	Inlet Velocity
v	Velocity
V	Volume

Subscripts

$(.)_i$	Einstein-notation

Superscripts

$\overline{(.)}$	Spatial Grid-filtering
$\widetilde{(.)}$	Spatial Test-filtering

Contents

1

Introduction

The subject of the present study is the flow around a low pressure turbine (LPT) outlet guide vane (OGV). The LPT comes at the rear end of the engine case next to the high pressure turbine (HPT) cascade(e.g., in case of a general two-spool engine). Immediately downstream of the LPT, the OGVs are positioned, which provide a structural connection between the aft bearing support, the main engine carcass and the aircraft attachment point. This is the structural function of the OGVs. In aerodynamic terms, their function is to de-swirl the swirling hot exhaust gas coming from the turbine rotors into an axial flow. The efficiency of gas turbine engines and the performance characteristics is said to increase with an increase in the core allowable temperature [1]. The motivation to push this temperature up requires to constantly look for better materials and cooling technologies for the rotor/guide vanes. Heat transfer study of the vanes thus becomes the core of the design process. Moreover, depending upon the operation point of the engine, the swirl angle could vary significantly leading to off-design conditions. Off-design conditions lead to a different thermal load and heat transfer prediction could be completely different. The blade life may be reduced to half, if the blade metal temperature prediction is off by just $10°C$ $(50°F)$ [2]. Thus, from the design point of view, computational and numerical study of the flow around the guide vanes and heat transfer prediction is of great importance.

Factors affecting heat transfer at the guide vane walls include boundary layer transition behaviour, flow separation and reattachment etc. While flow separation and reattachment are phenomena prominent in flow during off-design conditions, analysing the flow during on-design conditions requires capturing the boundary layer transition mechanism accurately. It has a significant effect on the heat transfer at the vane walls. Numerous studies on this mechanism have been carried out till date, both experimental and numerical. Computationally, it is very difficult to capture the transition at high free-stream turbulence (FST) levels, governed by non-linear interactions between boundary

layer and FST disturbances, termed as 'bypass transition'. One of the reasons being that the mechanisms governing the transition are not fully understood yet, due to the myriad of factors that come into play (discussed later). A universal mathematical model describing the (non-linear) growth mechanisms leading to transition is hence difficult to contrive. To get around this problem, efforts were made to isolate these governing factors and understand their individual effects. It was observed that such a transition takes place when two or more of these instability inducing factors interact amongst themselves; and it is the interaction of free-stream turbulence with the other instability inducing factors in the boundary layer that contributes to the growth of the non-linear modes predominantly. This is the reason why, in the presence of such high levels of free-stream turbulence, transition was reported to take place for flows with Reynolds number (Re) even lower than the critical Re computed using the classical linear stability theory. The linear stability theory only concerns exponentially growing instabilities in the boundary layer and does not consider the non-linear interaction due to FST.

Many of these aforementioned efforts were based on either full/direct numerical simulations (DNS) or Large eddy simulations (LES), non-modal linear stability analysis, linear and non-linear optimization techniques for largest energy growth of instability modes etc. Few of these studies will be discussed in Chapter 2. Historically, they have been performed only on simple geometries, since the aim had been to understand the physics/mechanism behind the transition. Recently, with the advancement in computational capability, researchers have been attracted towards performing LES over complex geometries, like turbine blades, as well ([3], [4], [5]). In the present study a similar effort has been made to simulate the transition in boundary layer over the turbine OGV using LES.

1.1 Previous work

The LPT OGV in the present study is designed by GKN Aerospace (previously Volvo Aero). OGVs in actual engines are arranged in a circular cascade and exhibit rotational periodicity. In this thesis, however, a linear cascade of OGVs is studied, since, the experiments done so far, and the basis of comparison of the current work, are on linear cascades and they provide a fairly good approximation to the circular one. The experimental studies by Hjärne [6] on such linear cascades at the department have so far served as the basis of subsequent experimental and computational studies. The current study is based on the experimental data obtained by Chenglong *et al.* at the department [7]. Chenglong *et al.* performed experiments at two operational settings – on-design and off-design conditions, with 25° and −25° incidence angle of the guide vanes respectively. Corresponding to this experiment, simulations based on RANS modelling approach was performed at GKN Aerospace [8]. Through the present thesis, it is the first time a computational study based on LES is carried out on these guide vanes; though only the on-design condition is studied.

1.2 Why LES?

Traditionally, for most of the engineering applications, RANS based modelling approaches have been employed to simulate transitional flows, due to their computational cost effectiveness. Broadly speaking, they can be divided into two categories. The first one is based on a simple 'point transition' approach whereby a switch is made (forced) between laminar and turbulent computations at a point determined either empirically or by an established correlation of relevant experimental or DNS data. In the second one, an extra transport equation for what is called an 'intermittency factor', γ, is solved. The intermittency factor represents the fraction of time the flow is turbulent. γ ranges from 0 to 1 while going from fully laminar to fully turbulent regime. A good overview of the early developments on these methods is given by Savill [9]. Recently, a third approach based on solving a separate transport equation for what is called as the 'Laminar Kinetic Energy' (LKE) has also been reported [10]. LKE represents the 'non-turbulent' stream-wise fluctuations in the pre-transitional boundary layer.

All spectral effects are lost in the time averaging process involved in RANS based approaches. However, 'bypass transition' is supposed to be very sensitive with respect to the spectral nature of the imposed FST. Hence it seems very unlikely that RANS based approaches could cope with transitional problems accurately. There are however some models that work well for specific problems. These models, based on the above mentioned approaches, consider only a few mechanisms or stages of transition. None of the models consider all the individual mechanisms and stages of transition. No model gives a reliable result for various combinations of FST intensity, Reynolds number and pressure gradients, and are found to be very sensitive to initial conditions, boundary conditions etc. LES, on the other hand, models only the smallest scales of motion, preserving the spectral nature of the larger energy containing eddies. In this respect, it is better than the RANS approach on the grounds of predicting transition more accurately. However, the bigger issue at hand is that the exact mechanism of transition is very debatable; while it is necessary to understand the physical mechanism of transition for better modelling of simulations. A good insight on the mechanism, based on previous research, will be provided in Chapter 2.

1.3 Aim and scope

Simulations at GKN Aerospace are done using two different models – one, the LKE (Laminar Kinetic Energy) model and the second, an intermittency based model. The LKE model showed better agreement with the experiments, once turbulence intensity at the inlet was scaled up to 8% from 3.5% in the experiments and the turbulent length scale was increased 20 times to $0.024m$. The onset of transition location did not match exactly and was off by a margin of 20%. In the present studies, LES is used for simulations in a hope to achieve a more realistic view of transition. The turbulent characteristics at the inlet are similarly scaled up, but not to the extent as mentioned above. The main

aim is to capture transition based on the scaled up turbulence characteristics; transition onset location is not of immediate concern in the present study. The main motivation comes from the LES study of boundary layer transition over a flat plate by Voke and Yang [11], who captured transition using a surprisingly coarse mesh. A major part of the thesis includes modifications made to the multigrid section of the solver, responsible for solving the pressure equation, based on the current boundary conditions. The report can be divided broadly into four parts:

- Elucidating the various mechanisms and stages involved in 'bypass transition'. – Chapter 2.
- Elaborating on LES, the SGS models to be used, and the pressure poisson equation. – Chapter 3.
- Mesh generation, case setup, and implementation of multigrid method in the code. – Chapter 4 and 5.
- Results, discussion and conclusion. – Chapter 6 and 7.

2

Boundary Layer Transition Theory

Whether it is the smoke coming out of a chimney or the flow in a river, most of the flows found in nature or in different engineering applications are chaotic or turbulent in nature. Depending upon the inertial and viscous properties of the wall-bounded flow, this nature – laminar or turbulent – can be very sensitive to perturbations in initial conditions, boundary conditions and material (surface) properties. In the presence of such perturbations, an initially laminar flow has the tendency to change into a more random or chaotic type of flow. This kind of evolution of flow, from laminar to fully turbulent, is referred to as *laminar-turbulent transition*. In most of the applications involving fluids, the ability to control the transition would greatly increase engineering efficiency and performance. However, even after more than a century of research, a complete understanding of this evolution process, especially the triggering mechanisms leading to turbulence has not been achieved.

The present study is focussed around the investigation of laminar-turbulent transition in the boundary layer of the flow in a turbine guide vane cascade. Such a flow comes under the category of *bounded shear flows* in *open systems*, which is characteristically different from free shear flows and closed systems. To understand the behaviour of such boundary layers (bounded, open), consider the flow over a semi-infinite flat 2-D plate. At the leading edge, the fluid particles close to the wall are slowed down due to viscosity, the closest one coming to rest instantaneously (no-slip condition). This results in the sudden increase in static pressure at the edge. As the fluid moves further downstream, additional layers parallel to the surface start getting affected due to viscosity. At a certain distance from the wall in normal direction the velocity reaches the free-stream value. This distance keeps increasing in the stream wise direction, as more and more layers of fluid start getting affected by the wall. It is referred to as the Boundary Layer. Flow in

the boundary layer near the leading edge is essentially laminar. After a certain distance downstream however, the flow in the boundary layer starts getting chaotic, marking the onset of transition. Further downstream, the flow gets completely turbulent. This is characterized by an increase in wall shear stress and heat transfer coefficient. Up until now, no mathematical model has been able to predict the transition Reynolds number for the flat plate accurately. The reason as stated earlier is the poor understanding of the triggering mechanisms.

In the following sections, based upon previous studies, different mechanisms and paths leading to this transition are reviewed briefly. More importance is given to the mechanism that the author thinks is crucial for the present study.

2.1 Paths of transition to turbulence

As mentioned in the beginning of this chapter, perturbations in initial conditions, boundary conditions or the inhomogeneities in surface (roughness) may enter the boundary layer and get amplified, resulting in creating instabilities. The development of such instabilities in a laminar flow is the first step towards the transition of turbulence. The

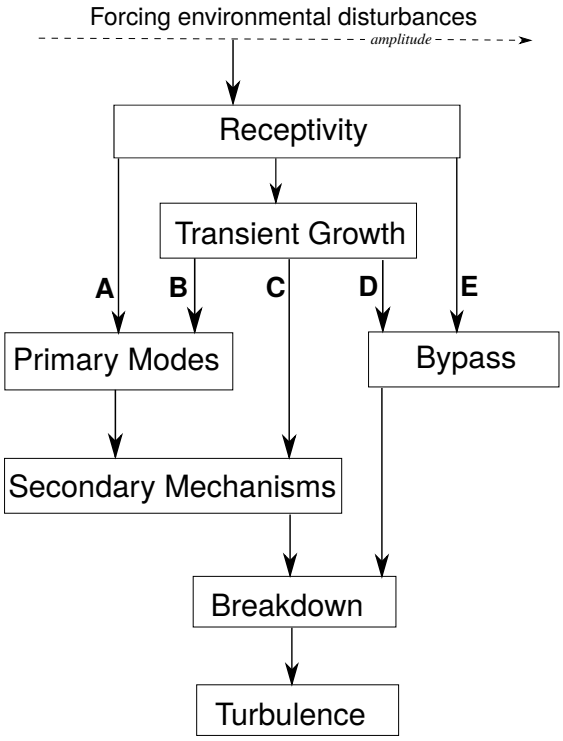

Figure 2.1: The paths from receptivity to transition [13]

interaction between external disturbances and the boundary layer instabilities is referred to as *receptivity*. Saric *et al.* [13] based on some earlier studies, gave a simplified scenario

for turbulence transition in external flows. Figure 2.1 depicts the same.

As the diagram in Figure 2.1 depicts, the initial external disturbance amplitude increases from left to right schematically. After the first step, *i.e.* receptivity, a number of different instabilities can occur independently or together depending on the Reynolds number, wall curvature, surface roughness or initial conditions and one of the five different paths shown is followed. Consider a scenario with very low free stream turbulence (FST) level at the inlet- generally equal to or below 1% of the mean flow. In such situations, path **A** is followed. The first stage in such type of transition is the development of two-dimensional Tollmien-Schlichting (TS) waves, which can be predicted by the modal/eigenvalue analysis of the linearized Navier-Stokes(NS) equations. These are exponentially growing instabilities evolving on large viscous time scales. As amplitude grows, the interactions take place on convective time scales (much smaller than viscous time scales), and are three-dimensional in nature. These interactions are then explained using the secondary instability theory. This is followed by the appearance of small-scale motions and the final stages of transition. Such a kind of transition is also called *natural transition*. Kachanov [14] has reviewed the theoretical and experimental work based on this type of transition.

A second scenario arises when the free stream turbulence (FST) level is high (generally higher than 1%). In such a case, transition will go into the non-linear interaction stage directly, and the linear instability stage marked by the formation and growth of TS waves is "bypassed". Such a transition is called *bypass transition* (path **D** and **E**). It is characterized by the appearance of streamwise elongated streaky structures of alternating high and low streamwise velocity in the laminar boundary layer, which grow in magnitude as they move downstream and finally lead to complete breakdown resulting in turbulence [15]. These streamwise structures (commonly referred to as *Klebanoff modes*) are low frequency oscillations and are very different from the exponentially growing perturbations (TS waves).

Paths **B**, **C** and **D** are based on the evolution of the initial boundary layer instability via what is called as the *transient growth* mechanisms. Studies on transition via *transient growth* mechanisms are based on non-modal analysis of the linearized NS equations, contrary to the modal analysis performed for the evolution of TS waves. An extensive review on the nonmodal stability analysis can be found in an article by Schmidt [16]. Most of the mechanisms of bypass transition proposed so far follow the path **D**. This will be discussed more extensively in the next section.

2.2 Bypass-transition mechanisms

Occurrence of streamwise elongated structures with alternating positive and negative streamwise disturbance velocities in laminar boundary layers subjected to FST was first observed by Klebanoff [17]. According to his observations, amplitude of the peak

response of such structures increased in proportion to the FST amplitude and boundary layer thickness. Later, Kendall too observed large spanwise variations in streamwise velocity in the pre-transitional boundary layer subjected to FST in his experimental study [18]. He termed these structures, *Klebanoff modes*. They are not modes in strict mathematical sense as they do not represent solution to an eigenvalue problem. They are usually depicted in terms of rms profiles of streamwise velocity in the boundary layer. A thorough experimental study was performed by Roach *et al.* [19] on bypass transition in a zero pressure gradient boundary layer, which is used extensively by other researchers for comparative studies.

2.2.1 Mechanisms based on transient growth (paths C and D)

Receptivity is the interaction of free-stream disturbances with a laminar boundary layer and is the first step towards transition to turbulence. In case of 'bypass' transition, it is associated with the appearance of streamwise streaks in the boundary layer. For inviscid flows, the streamwise velocity can grow linearly in time in the presence of a distubance with no streamwise variation. This is ascribed to the lift-up and vortex-stretching mechanism or more accurately to the vortex tilting mechanism. The normal vorticity increases in time due to the tilting of cross-stream (spanwise) vorticity by the perturbation strain rate in spanwise direction (this disturbance can be viewed as a streamwise vortex). Since the disturbance is elongated in the streamwise direction due to the mean shear, the final effect can be seen as streaks with high and low stramwise velocity fluctuations. A good description can be found in the introduction of the article by Butler and Farrell [20]. It is believed that in the presence of viscosity though, such inviscid amplifications eventually decay after a short time or short streamwise distance. This phenomenon is termed as 'transient growth'. It is then possible for a sufficiently amplified disturbance, before decay sets in, to trigger non-linear interactions and cause breakdown to turbulence.

Mathematically, this transient energy amplification is not due to the behaviour of a single eigenmode of the linearized disturbance equation as found in exponentially growing TS waves. It is caused by the superposition of several modes; hence, called non-modal growth as well. It is believed to be caused by the non-normal nature of the linear operator pertaining to the linearized disturbance equation. Such growth is larger for disturbances mainly exhibiting spanwise periodicity, that is having low frequency or streamwise wavenumbers. A detailed explanation can be found in the colloquium by Grossmann on shear flow turbulence [21].

The transient growth mechanism is linear in nature and has been studied extensively using optimization techniques. The initial disturbance able to induce maximum transient growth at a given time is referred to as *optimal*. Butler and Farrell [20] using variational methods, found the optimal perturbation responsible for the maximum transient growth in a boundary layer for Couette and Poiseuille flows. They found that perturbations in the form of streamwise/longitudinal vortices (correspond to zero-streamwise wavenum-

ber) are responsible for inducing the greatest energy growth in the laminar boundary layer in the form of powerful streamwise streaks, that can be related to the Klebanoff modes found in the pre-transitional boundary layer in the 'bypass' transition case. Andersson *et al.* [22] and Luchini [23] in separate studies formulated a spatial instability problem unlike the temporal instability problem by Butler and Farrell; they also found that the optimal perturbation consisted of a pair of counter rotating streamwise vortices outside the boundary layer. Luchini also found that the shape of the streaks in the pre-transitional boundary layer tends to be attracted towards the shape of the optimal perturbation (Klebanoff modes), even for non-optimal initial perturbations. The shape was found to be insensitive to a wide range of wavenumbers, frequencies and shape of the initial perturbation.

Several experimental and numerical studies have observed transition due to the presence of such streaks. Matsubara *et al.* [24] did an extensive review of experimental studies on disturbance growth inside the boundary layer. Their experiments corroborated well with the linear non-modal growth mechanism of the boundary layer streaks. Jacobs and Durbin [25] performed Direct Numerical Simulation (DNS) of flow over a flat plate. Based on an earlier proposition [26], they constructed the turbulence inflow by expanding the FST as a sum of spanwise and temporal fourier modes, multiplied by wall-normal Orr-Sommerfeld modes. Only the continuous spectrum of the latter was considered due to their inherent property of being sinusoidal in the free-stream and approaching to zero near the wall. In an earlier study [27], Jacobs and Durbin had explained the *shear sheltering mechanism*. They had observed that disturbances convected with free-stream velocity did not couple to the slower fluid in the shear layer near the wall. Penetration depth of such disturbances was found to be inversely proportional to their frequency and the Reynolds number based on the distance from the leading edge. In the DNS study [25], they conclude that streaks are an implicit property of the boundary layer. Though the amplitude of the FST is a crucial input for transition, actual frequency selection takes place inside the boundary layer and is not sensitive to the details of inlet disturbance spectrum. The process is non-linear since the dominant frequencies found inside the boundary layer were much smaller than the ones prescribed at the inlet. Brandt *et al.* [28] in their DNS study of a flat plate boundary layer, also used the continuous spectrum of the Orr-Sommerfeld equation to generate inflow boundary condition similar to Jacobs and Durbin, but also included the Squire modes for the wall-normal vorticity. They found that the transition onset moved upstream with increasing the FST length scale. However, like in the Jacobs and Durbin study [25], the spanwise scale of the streaks inside the shear layer was found to be highly insensitive towards the details of inlet turbulence (FST). So, probably the scales at the inlet spectrum are important in the next phase of transition, *i.e.*, the breakdown phase. Jonáš *et al.* [29] performed experiments on flat plate boundary layer, and also concluded that the onset of transition moved upstream with increasing FST length scale.

Brandt *et al.* [28] also conclude that for receptivity, linear mechanism is most rel-

evant if the FST contains low-frequency disturbances, whereas, non-linear mechanism takes over if the FST contains high-frequency disturbances. Earlier Berlin and Henningson [30] had proposed a non-linear receptivity mechanism based on their spectral DNS study of Blasius flow with both temporal and spatial formulations. According to them, non-linear mechanism is responsible for generating wall-normal perturbations associated with streamwise vortices inside the boundary layer, which on interacting with the boundary layer shear produce the streamwise streaks. They also conclude that for receptivity, at low FST intensity levels linear mechanism dominate, whereas non-linear mechanism plays important role at higher FST levels. At moderate disturbance levels, both mechanisms produce streaks of similar strength. But owing to the non-linear mechanism it is possible for the free-stream to continuously force streaks inside the boundary layer even downstream of the leading edge. It should be noted that the growth of streaks is still supposed to be based on linear transient mechanism; it is only the appearance of streaks, that could be linear or non-linear. The importance of wall-normal velocity in the free-stream for inducing transition was also emphasized by Voke and Yang [11] in their LES study of flow over a flat plate.

Zaki *et al.* [31] analyzed the Orr-Sommerfeld/Squire eigenvalue problem and showed that the penetration depth of a free-stream disturbance inside a boundary layer shear depends on four parameters. The penetration is inversely proportional te frequency of disturbance, Reynolds number, and the local mean shear at the wall. It increases with increasing wall-normal wavenumber. But they also pointed out that by increasing the wall-normal wavenumber, the decay rate also increases and the disturbance does not persist far downstream of the leading edge. A coupling coefficient was defined that depicted the local interaction of continuous Orr-Sommerfeld modes and the boundary layer. It represented the penetration ability of the modes in the boundary layer and also its ability to generate streaks. Not all penetrating modes generated streaks; the ones with high decay rate failed to do so, *e.g.* disturbances with high wall-normal wavenumber. Disturbances with low frequencies and small wall-normal wavenumbers had higher coupling coefficients.

Leading edge effects were not considered in the studies discussed so far. Most of the studies on transient growth assumed parallel flow. As a result they could not capture the effect of leading edge, since the flow around a leading edge is non-parallel. The same can be said for the numerical studies discussed so far, which had the inflow plane for simulations situated downstream of the leading edge. Zaki and Durbin [31] consider a leading edge, but argue that at the leading edge, as boundary layer thickness $\delta \to 0$, all modes act as low frequencies and become penetrating; but since $Re_x \to 0$ (Re based on distance from leading edge), they also decay rapidly. They conclude that the coupling leading to boundary layer streaks and transition is local, and occurs downstream of the leading edge. The non-linear method discussed by Berlin and Henningson [30] forced streaks in the boundary layer locally even downstream of the leading edge. Goldstein and Wundrow [32] in their analysis consider the leading edge and show that FST containing

wake like disturbances, corresponding to wall-normal vortical structures, get stretched and tilted around the leading edge and transform into low frequency modes corresponding to streamwise aligned vortices. These vortices then penetrate in the boundary layer to produce streaks. Leading edge just enhances the growth of Klebanoff modes inside the boundary layer; the mechanism to transition still remains the same. Nagarajan *et al.* [33] carried out simulations on a flat plate boundary layer with a blunt elliptical leading edge. They observe that a blunter leading edge, at given free stream conditions, exhibits earlier onset and completion of transition. They also find the same mechanism in play around the leading edge as observed by Goldstein and Wundrow– stretching and tilting of vortices around the leading edge. But according to them, a blunter leading edge results in a completely different mechanism to transition and will be discussed later.

The Pressure gradient has also a significant effect on the receptivity process. Zaki *et al.* [34] in their numerical simulations observed that adverse pressure gradient (APG) results in a higher shear close to the boundary as compared to zero or favourable pressure gradient cases (ZPG and FPG respectively). As a result, the Orr-Sommerfeld modes constituting the inflow FST are expected to penetrate less in the APG case than in the other cases, owing to shear sheltering [31]. But instead of transition being delayed or averted, it is earlier and faster than in the latter two cases. The reason is that APG induces stronger streaks in the boundary layer than in ZPG or FPG flows, thus making it more succeptible to the FST forcing.

Streak break-down and secondary instabilities: The streamwise elongated unsteady streaks in the boundary layer are the main driving source of bypass transition. Mechanisms driving the conversion of streaks into turbulent spots and subsequent break-down have been an important aspect of bypass transition studies. Jacobs and Durbin [25] observe that streaks with negative streamwise fluctuation ($u' < 0$), termed as negative jets, are responsible for the formation of turbulent spots. They are present predominantly at the upper boundary of the shear layer, and are continuously in contact with the high frequency free-stream disturbances outside the boundary layer. Only some of these streaks develop to spots, implying that the coupling of these jets to the free-stream eddies is essential. Positive jets, predominant close to the surface of the plate, do not undergo instability. Brandt *et al.* [28] observe that streak breakdown and turbulent spot formation is caused by either of two types of instability modes of low-speed streaks (negative jets). The sinuous mode, characterized by streak oscillations in the spanwise direction, was observed more frequently than the varicose mode of instability, which is driven by the wall-normal shear. The sinuous mode instability is similar to the backward jet mechanism of Jacobs and Durbin [25]. Zaki *et al.* [31] in their DNS study used a pair of inflow modes, one with high coupling coefficient (presumably low frequency), and the other a weakly coupled mode (high frequency) and observe that it was sufficient to trigger transition. The former generates streaks inside the boundary layer. The low-speed streaks (negative jets) lift towards the edge of the boundary layer, which are then acted upon by fluctuations due to the latter, the (high-frequency) weakly coupled mode. The

latter is unable to penetrate the shear layer and is present in the free-stream. Some of these jets get intensified and burst into turbulent spots. This is also similar to the mechanism observed by Jacobs and Durbin.

There are many more studies based on streak growth which are not discussed here. The point the author wants to make is that linear growth or transient growth of streaks is not alone sufficient for triggering transition, though they seem to be necessary. Non-linear forcing provided by the FST and its interaction with the streaks is an important condition to induce transition.

2.2.2 Mechanism 'bypassing' transient growth (path E)

Nagarajan *et al.* [33] observe in their DNS study that the same inflow turbulence field leads to different paths to transition depending upon the leading edge geometry. Also, there is a change in the location of transition onset consequently. Spot precursors responsible for transition were identified to be wavepacket like disturbances originating at the leading edge (blunt). They inhabited the lower part of the boundary layer, in contrast to the sinuous streak instabilities discussed earlier, which were found in the upper part, corresponding to the low-speed streaks. Vortices aligned normal to the wall get stretched around the leading edge resulting in localized regions of streamwise vorticity inside the boundary layer, which grow as they convect downstream. Ovchinnikov *et al.* [35] studied the effect of FST length scales and leading edge on bypass transition. For FST length scales comparable to the boundary layer thickness at the onset of transition, δ_{99}, the transition followed the Klebanoff mode mechanism discussed earlier. But for higher FST length scales, comparable to almost $7\delta_{99}$, the transition followed a different path. They observe that wavepacket like disturbances in streamwise direction act as spot precursors that lead to transition. They are associated with spanwise vortical structures in boundary layer in contrast to streamwise ones in the simulations of Nagarajan *et al.* [33]. Initially in spanwise direction, the vortices subsequently reorient themselves partially in streamwise direction. The result is either a horseshoe/hairpin/Λ vortex (two legs) or quasi-streamwise vortex (one-leg). These structures finally develop into spots and subsequently break down to turbulence. They also find that wavepackets appear in wall-normal velocity component as compared to the spanwise component in the simulations of Nagarajan *et al.* and that they are not confined to the lower part of the boundary layer close to the wall, as was observed by the former. The possible explanation for such difference was attributed to the higher Re (based on FST integral length scale) in the study of Ovchinnikov *et al.* and also the higher FST intensity in their study. Wu and Moin [36] performed DNS for a spatially evolving turbulent zero pressure gradient boundary layer over a smooth flat plate. According to their flow visualizations, boundary layer streaks appeared to be merely a kinematic feature, appearing as a result of lift up mechanism. They were not found to be responsible for transition. The non-linear development of obliquely oriented Λ-vortices into hairpin packets was observed to be responsible for the breakdown into transition. However, receptivity of such disturbances inside the boundary layer was not discussed. Recently, Cherubini *et al.* [37] proposed

a purely non-linear scenario of (bypass) transition in boundary layer, justifying the preponderance of hairpin structures observed by Wu and Moin [36] in their transitional boundary layer. Using non-linear optimization of the energy growth at short time, they identified the smallest flow structure, called the *minimal seed perturbation*, responsible for inducing turbulence in the boundary layer. In a more recent article, Cherubini *et al.* [38] conclude that transition in a flat plate boundary layer in the presence of FST, follows a purely non-linear route characterized by the formation of hairpin/Λ vortices, when turbulent intensity and turbulent length scale of the FST are very high (for $I > 4.5\%$ and $l > 20$). For, lower intensities and length scales of the FST, the transition was said to follow the traditional streak mechanism (transient growth and secondary instability leading to break-down).

2.3 Previous studies using LES and mesh resolution issues

One of the earliest works on boundary layer transition using LES includes the simulations on flat plate boundary layer by Voke and Yang [11]. They observed transition on a very coarse mesh with resolution based on wall units as, $\Delta x^+ = 80$, $\Delta z^+ = 14$ and $\Delta y^+ = 1$ at the wall to 80 beyond the boundary layer. The wall units were computed based on friction velocity just after transition. More recently Collado Morata *et al.* [4] did heat transfer studies on high pressure turbine blades in the presence of high free stream turbulence levels using LES and ovserved transition in boundary layer. Their mesh resolution for structured LES was also fairly coarse in the streamwise direction. They had $\Delta x^+ \sim 150$, $\Delta z^+ \sim 25$ and $y^+ \sim 1$ at the wall. Medic *et al.* also performed a similar heat transfer study on the turbine cascade using LES. Their streamwise and spanwise resolution was fairly lower than that of Collado Morata *et al.* ($\Delta s^+ < 50$, streamwise resolution and $\Delta z^+ < 10$, spanwise resolution).

The optimal mesh resolution required for studying transitional flows is therefore debatable. Kaltenbach and Choi [39] performed LES of flow around an airfoil, though, did not study transition. They had streamwise resolution, Δx^+ ranging from, approximately, 400 at the leading edge to 100 near the trailing edge and spanwise resolution, Δz^+, between 130 and 13 near leading and trailing edge respectively. In the present simulations the resolution is similar to that of Collado Morata *et al.* and will be discussed in Chapter 4.

3

Governing Equations and Solution Methods

Application of conservation of momentum, along with energy and mass conservation on a portion of fluid volume, called control volume, leads to the Navier-Stokes (NS) equations. The NS equations in conservative form in the absence of body forces for an incompressible and isotropic Newtonian fluid can be written as:

$$\frac{\partial v_i}{\partial x_i} = 0 \tag{3.1}$$

$$\frac{\partial v_i}{\partial t} + \frac{\partial v_i v_j}{\partial x_j} = -\frac{1}{\rho}\frac{\partial p}{\partial x_i} + \nu \frac{\partial^2 v_i}{\partial x_j \partial x_j} \tag{3.2}$$

The energy equation (heat transfer equation) in the absence of heat sources for such a fluid, neglecting the viscous heating effect (dissipation function) can be expressed as:

$$\frac{\partial \theta}{\partial t} + \frac{\partial v_j \theta}{\partial x_j} = \alpha \frac{\partial^2 \theta}{\partial x_j \partial x_j} \tag{3.3}$$

The three equations above represent the continuity, momentum conservation and energy conservation equations (θ: temperature) respectively. The exact analytic solution of these equations is extremely difficult to achieve. The possible way to get around the solution is to solve it numerically using iterations performed on the discretized equations. One way is to solve the time averaged equations, wherein, the extra terms appearing out of averaging are modelled: the RANS method. Another way is to resolve the whole range of temporal and spatial scales, without the need for modelling: called the DNS. This requires a very fine grid and for larger Reynolds number the computational cost goes up so high that it is practically not possible for a lot of problems. These two ways are the two extremes of the spectrum based on computational cost. There are many

middle ways. One of them is LES, wherein the larger energy containing motions are resolved and the effect of smaller ones are modelled.

3.1 Large Eddy Simulations

As said earlier, in LES, the larger scales are resolved and smaller ones are modelled. The first step in LES is filtering in which the flow variable (say ϕ) is decomposed into the sum of a filtered/resolved component ($\bar{\phi}$) and the residual/SGS(sub-grid scale) component (ϕ'). Details about filtering operations can be found in [40]. In this study, a simple volume-average box filter is used where the filter-width ($\bar{\Delta}$) is simply taken as the local grid size [$\bar{\Delta} = (\Delta V_{IJK})^{1/3}$]. Equations (3.1)–(3.3), after the filtering operation give rise to a set of equations with certain additional terms arising due to filtering.

$$\frac{\partial \bar{v}_i}{\partial x_i} = 0 \tag{3.4}$$

$$\frac{\partial \bar{v}_i}{\partial t} + \frac{\partial \bar{v}_i \bar{v}_j}{\partial x_j} = -\frac{1}{\rho}\frac{\partial \bar{p}}{\partial x_i} + \nu \frac{\partial^2 \bar{v}_i}{\partial x_j \partial x_j} - \frac{\partial \tau^r_{ij}}{\partial x_j} \tag{3.5}$$

$$\frac{\partial \bar{\theta}}{\partial t} + \frac{\partial \bar{\theta} \bar{v}_j}{\partial x_j} = \alpha \frac{\partial^2 \bar{\theta}}{\partial x_j \partial x_j} - \frac{\partial \tau_{\theta j}}{\partial x_j} \tag{3.6}$$

where, τ^r_{ij} represents the *residual-stress tensor*, defined as $\tau^r_{ij} \equiv \overline{v_i v_j} - \bar{v}_i \bar{v}_j$ and $\tau_{\theta j}$ represents the *residual heat flux* and defined analogous to τ^r_{ij}.

The next step is to obtain closure by modelling the residual flux terms. First, consider the residual flux term in the momentum equation (eq.(3.5)). It is modelled based on certain assumptions. The majority of them are based on the eddy-viscosity modelling approach – *Boussinesq assumption* in case of RANS modelling. In this study two such models are used for performing LES – the Smagorinsky model and the Dynamic model.

3.1.1 Smagorinsky model

This model forms the basis of all other eddy-viscosity models. Like all other eddy viscosity models used for RANS, it assumes the *Boussinesq hypothesis* and the deviatoric part of the residual-stress tensor is proportional to the filtered strain rate tensor ($\overline{S}_{ij}$),

$$\tau^r_{ij} - \frac{1}{3}\tau^r_{kk}\delta_{ij} = -2\nu_r \overline{S}_{ij} \tag{3.7}$$

The constant of proportionality ν_r is the residual viscosity, also called the SGS viscosity and needs be modelled. By analogy to the mixing-length hypothesis, the eddy-viscosity is modelled as,

$$\begin{aligned} \nu_r &= l^2_{smg} \left|\bar{S}\right| \\ &= l^2_{smg} \sqrt{2\overline{S}_{ij}\overline{S}_{ij}}, \end{aligned} \tag{3.8}$$

where, l_{smg} represents the *Smagorinsky lengthscale* and taken as proportional to the filter-width $\bar{\Delta}$, such that

$$l_{smg} \equiv C_s \bar{\Delta},$$

where, C_s is the *Smagorinsky coefficient*.

This model gives a high residual viscosity at the wall, owing to high velocity gradients (hence, high $\left|\bar{S}\right|$) in this region. This is not accurate since the SGS turbulent fluctuations go to zero near a wall. In order to dampen the eddy-viscosity, the RANS length scale is used as an upper limit in the present solver. Thus,

$$\bar{\Delta} = min\left\{\left(\Delta V_{IJK}\right)^{1/3}, \kappa n\right\}, \tag{3.9}$$

where, n is the distance to the nearest wall.

3.1.2 Dynamic model

With a single universal value for the Smagorinsky constant C_s, it is difficult to represent different flow regimes. It can be different for different flow regimes [40]. The Dynamic Model provides a way to determine the coefficient locally and dynamically (variable of time and space) as opposed to the constant value of Smagorinsky. To achieve this, a second filtering operator is introduced with a larger width than the grid filter ($\bar{\Delta}$). This filter is called the *test filter*. The test filter-width, $\widetilde{\bar{\Delta}} = r\bar{\Delta}$, where $r > 1$. The optimal value is found to be 2 [41]. The filtered NS equation at the second level (test-filtered) is written as,

$$\frac{\partial \widetilde{\bar{v}}_i}{\partial t} + \frac{\partial \widetilde{\bar{v}}_i \widetilde{\bar{v}}_j}{\partial x_j} = -\frac{1}{\rho}\frac{\partial \widetilde{\bar{p}}}{\partial x_i} + \nu \frac{\partial^2 \widetilde{\bar{v}}_i}{\partial x_j \partial x_j} - \frac{\partial T_{ij}}{\partial x_j} \tag{3.10}$$

This is similar to (3.5), except that the variables here are test filtered. Also, the last term in both the equations are different. For simplicity, the τ_{ij}^r in (3.5) will be referred to as τ_{ij} from now on. The residual stress tensors from both equations are,

$$\tau_{ij} = \overline{v_i v_j} - \bar{v}_i \bar{v}_j, \tag{3.11}$$

and

$$T_{ij} = \widetilde{\overline{v_i v_j}} - \widetilde{\bar{v}}_i \widetilde{\bar{v}}_j \tag{3.12}$$

Assuming that the same functional form (as in Smagorinsky model (3.7)) can be used for parametrizing both T_{ij} and τ_{ij}, let M_{ij} and m_{ij} represent the deviatoric part of the stresses T_{ij} and τ_{ij} respectively. Thus,

$$\tau_{ij} - \frac{\delta_{ij}}{3}\tau_{kk} = m_{ij} = -2C\overline{\Delta}^2 |\overline{S}| \overline{S}_{ij}, \tag{3.13}$$

and

$$T_{ij} - \frac{\delta_{ij}}{3}T_{kk} = M_{ij} = -2C\widetilde{\bar{\Delta}}^2 |\widetilde{\bar{S}}| \widetilde{\bar{S}}_{ij}, \tag{3.14}$$

where

$$\widetilde{\overline{S}}_{ij} = \frac{1}{2}\left(\frac{\partial\widetilde{\overline{v}}_i}{\partial x_j} + \frac{\partial\widetilde{\overline{v}}_j}{\partial x_i}\right), \qquad |\widetilde{\overline{S}}| = \sqrt{2\widetilde{\overline{S}}_{ij}\widetilde{\overline{S}}_{ij}} \tag{3.15}$$

Here, C is equivalent to C_s^2 in the Smagorinsky model.

It was recognized by Germano that T_{ij} and τ_{ij} are related by a relation (*Germano identity*),

$$\begin{aligned}\mathcal{L}_{ij} &= T_{ij} - \widetilde{\tau}_{ij} \\ &= \widetilde{\overline{v}_i\overline{v}_j} - \widetilde{\overline{v}}_i\widetilde{\overline{v}}_j,\end{aligned} \tag{3.16}$$

where, $\mathcal{L}_{ij}$ represents the resolved components of turbulent stress associated with scales of motion between the test scale and the grid scale and it can be computed explicitly. The consistency between (3.13) and (3.14), however, depends upon the proper choice of C. So, the whole model boils down to finding that C, which is locally and dynamically optimal. In order to achieve this, Germano proposed a method, wherein, (3.13) and (3.14) are substituted in (3.16) and then is contracted wtih $\overline{S}_{ij}$ [41]. A better method, which yields a computationally more stable value of C was developed shortly by Lilly [42]. The solver in the present simulations use the formulation provided by Lilly.

Substituting equations (3.13) and (3.14) in (3.16) and assuming negligible variation of C in the test-filter volume,it can be seen that,

$$\mathcal{L}_{ij} - \frac{\delta_{ij}}{3}\mathcal{L}_{kk} = 2C\mathcal{M}_{ij}, \tag{3.17}$$

where,

$$\mathcal{M}_{ij} = \overline{\Delta}^2\widetilde{|\overline{S}|\overline{S}_{ij}} - \widetilde{\overline{\Delta}}^2|\widetilde{\overline{S}}|\widetilde{\overline{S}}_{ij} \tag{3.18}$$

To calculate $\mathcal{M}_{ij}$, Lilly suggested the least-squares approach, and C is evaluated as

$$C = \frac{1}{2}\frac{\mathcal{L}_{ij}\mathcal{M}_{ij}}{\mathcal{M}_{ij}\mathcal{M}_{ij}} \tag{3.19}$$

It was realized that the computed value of C may vary wildly in time and space, since it is an instantaneous and local quantity. This in turn, might lead to numerical instabilities. In order to avoid this, C is averaged along the homogeneous directions of the flow.

Piomelli *et al.* [43] studied the budget terms of the resolved energy equation that included the SGS dissipation term from DNS of transitional and turbulent channel flow. According to them, to model transitional channel flow appropriately, it was necessary to consider the backscatter effects (the inverse transfer of energy from small to large scales). As mentioned earlier, the present work aims to study the boundary layer transition over a turbine guidevane, and since, the Dynamic SGS model treats the backscatter effect well, it was decided to use the model for the present study as well.

3.2 Solving for the temperature field

Now, consider the residual-heat flux term $\tau_{\theta j}$ in equation 3.6. There are ways of modelling it by writing a separate transport equation involving the term as in [44]. The present work doesn't delve into this. Instead, assuming that the thermal boundary layer will develop similar to the velocity boundary layer, the residual flux term is modelled based on the residual/SGS viscosity, ν_r. Drawing analogy from the eddy-viscosity model in equation 3.7 and by introducing a residual thermal eddy-diffusivity α_r, the residual flux term in the temperature equation can be modelled as,

$$\tau_{\theta j} = -\alpha_r \frac{\partial \bar{\theta}}{\partial x_j}. \tag{3.20}$$

Similar to the definition of molecular Prandtl number Pr, a turbulent Prandtl number Pr_t is introduced as the ratio between the two residual diffusivities.

$$Pr_t = \frac{\nu_r}{\alpha_r}$$

Thus, by modelling only the residual/SGS viscosity, both the momentum and thermal equations are solved. It is taken to be around 0.7 to 0.9 in general.

3.3 Solving for the pressure field: PPE

In case of an incompressible flow, there is no explicit equation for solving pressure. Pressure is involved in the momentum equations (3.2) and in general, it is solved indirectly by making use of the continuity equation (3.1). For example, in SIMPLE algorithm a pressure correction equation derived from the continuity equation is solved and used to update the velocity field. In the present case, pressure is computed directly by solving a Pressure Poisson equation (PPE). The consistent PPE is derived by taking divergence over the momentum equation (3.2):

$$\frac{1}{\rho}\frac{\partial^2 \bar{p}}{\partial x_i \partial x_i} = -\frac{\partial^2 \bar{v}_i}{\partial x_i \partial t} - \frac{\partial^2 \bar{v}_i \bar{v}_j}{\partial x_i \partial x_j} + \nu \frac{\partial^3 \bar{v}_i}{\partial x_i \partial x_j \partial x_j} - \frac{\partial^2 \tau^r_{ij}}{\partial x_i \partial x_j} \tag{3.21}$$

By applying proper boundary conditions, and imposing the divergence of velocity field to go to zero – the continuity eqation – the above equation can be solved. In the present numerical method, an intermediary velocity field from the NS equations devoid of the implicit Pressure gradient term is first solved. A similar PPE as above is formulated by imposing the requirement of continuity on the correct velocity field. More about this formulation and the whole projection method to solve the system of equations is explained in [45].

The effectiveness of the afore mentioned fractional step projection method mentioned is based on the efficiency of the PPE matrix solver. To solve the PPE, a Geometric Multigrid (GM) algorithm is employed, which is explained in brief in the next section.

3.4 Geometric Multigrid Method

To any system of equations, especially non-linear, when solved using iterative methods, the solution consists of two kinds of errors. One is truncation error, arising due to discretization scheme used or the quality of mesh used (coarse or fine). The other one is called algebraic error, which is the difference between the exact solution and the iterative solution. The first kind of error is reduced either by using a higher order discretization scheme or by refining the mesh. The second kind of error reduces with the number of iterative sweeps. Multigrid techniques are precisely used for the latter kind of errors – to accelerate the rate at which the error can be reduced. Upon Fourier decomposition, error can be said to be consisting of different components/modes of different wavelengths. Of theses modes, the modes with shorter wavelength smooth out within a few iterations, while the longer wavelength components require a lot of iterations, rendering the process computationally expensive. The smoothing effects on long and short wavelength error modes are neatly explained in [46]. In the present case/problem, a geometric multigrid technique is used to solve the Pressure Poisson equation (PPE). This technique is very efficiently implemented in the CALC-LES code. The subsequent subsections explain the theory in short.

3.4.1 Full Approximation Storage: FAS

The Full Approximation Storage (FAS) scheme is a multigrid algorithm formulated for a non-linear problem, but it can be generalized to include a linear problem. The algorithm to solve the linear problem can be found in the book by Versteeg and Malalasekera [47]. To start with FAS scheme, consider a non-linear system of equations,

$$\mathbf{A}(\Phi) = \mathbf{f}, \tag{3.22}$$

where, Φ is the true solution of the system and $\boldsymbol{\psi}$, an intermediate solution to it after a couple of iterations/sweeps. The algebraic error $\mathbf{e}$ is then defined as

$$\mathbf{e} = \Phi - \boldsymbol{\psi}, \tag{3.23}$$

and the residual equation can be written as,

$$\mathbf{A}(\Phi) - \mathbf{A}(\boldsymbol{\psi}) = \mathbf{r} \tag{3.24}$$

It can be easily seen that for a linear $\mathbf{A}$, the equation becomes $\mathbf{A}(\mathbf{e}) = \mathbf{r}$. But in this case (non-linear), this doesn't hold true. A two-grid version of the FAS scheme can be explained in the following steps:

- **Fine grid iterations:** In general it starts with a few iterations at the finest grid with mesh spacing h. This step removes the high frequency error components. The fine grid residual $\mathbf{r}^h$ is computed. This step is also called **Pre-smoothing**.

- **Restriction:** Both the fine grid residual and the intermediate solution vector are restricted to the coarse grid mesh using the restriction operator $\mathbf{I}_h^{2h}$.

$$\begin{aligned}\mathbf{r}^{2h} &= \mathbf{I}_h^{2h}\mathbf{r}^h \\ &= \mathbf{I}_h^{2h}(\mathbf{f}^h - \mathbf{A}^h(\boldsymbol{\psi}^h))\end{aligned} \tag{3.25}$$

  And similarly,

$$\boldsymbol{\psi}^{2h} = \mathbf{I}_h^{2h}\boldsymbol{\psi}^h \tag{3.26}$$

- **Relaxation at the coarser level:** Substituting the above two terms in the coarse grid formulation of equation (3.24) gives,

$$\begin{aligned}\mathbf{A}^{2h}(\Phi^{2h}) &= \mathbf{A}^{2h}(\mathbf{I}_h^{2h}\boldsymbol{\psi}^h) + \mathbf{I}_h^{2h}(\mathbf{f}^h - \mathbf{A}^h(\boldsymbol{\psi}^h)) \\ &= \widetilde{\mathbf{f}}^{2h}\end{aligned} \tag{3.27}$$

  Equation (3.27) is solved for Φ^{2h}. Then using the error equation (3.23) for the coarse grid, $\mathbf{e}^{2h}$ is computed.

$$\mathbf{e}^{2h} = \Phi^{2h} - \mathbf{I}_h^{2h}\boldsymbol{\psi}^h \tag{3.28}$$

  Unlike in the linear case, here the system is not solved for $\mathbf{e}^{2h}$ directly. Since a full approximation (of Φ^{2h}) is stored at each level, unlike in the linear case (where only the correction, $\mathbf{e}^{2h}$ is stored), this method is named as *full approximation storage*.

- **Prolongation:** The error $\mathbf{e}^{2h}$ found in this way at the coarse mesh is transferred back (called Prolongation) to the fine mesh using an interpolation operator $\mathbf{I}_{2h}^h$,

$$\widetilde{\mathbf{e}}^h = \mathbf{I}_{2h}^h\mathbf{e}^{2h} \tag{3.29}$$

  The difference between $\widetilde{\mathbf{e}}^h$ and $\mathbf{e}^h$ is the lower frequency components; they are absent in the former.

- **Correction and final iterations:** Finally, the prolongated error vector $\widetilde{\mathbf{e}}^h$ is used to correct the intermediate fine grid solution $\boldsymbol{\psi}$ and a few more iterations are performed to smoothen out the error that might have occurred due to restriction and prolongation. Hence, it is called **Post-smoothing**.

$$\boldsymbol{\psi}^h \leftarrow \boldsymbol{\psi}^h + \widetilde{\mathbf{e}}^h \tag{3.30}$$

This is a typical two-grid multigrid method. Based upon this method, a lot of recursive schedules/schemes have been developed, like V-cycles, W-cycles, F-cycles scheme or the FMG scheme, the details of which are not discussed here. The implementation of the FAS scheme is explained in Chapter 5.

4

Geometry and Mesh Generation

4.1 Geometry and computational domain

The given geometry is a typical aerofoil profile in two-dimensions, extruded in the third direction. The profile of cross-section of the guide-vane is shown in Figure 4.1. The

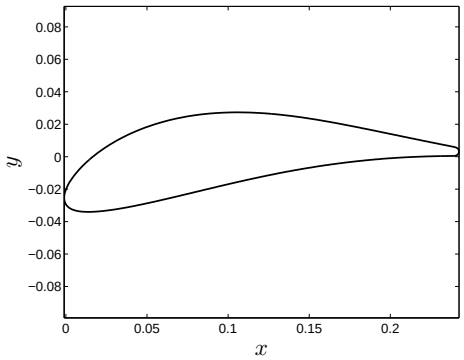

Figure 4.1: Geometry profile of the guide-vane

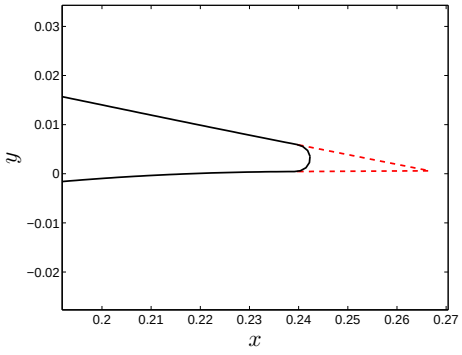

Figure 4.2: Trailing edge extrapolation. — given geometry ; – – extrapolated part

trailing edge of this profile is circular, which is made sharp by extrapolating the suction side and pressure side curves further downstream till they coincide. This operation is driven by the need of having a well-defined edge (or point in 2-D) to define the periodic boundaries of the cascade domain. The extrapolated part can be seen in red in Figure 4.2, which shows the geometry magnified near the trailing edge. The length of the extrapolated part is around 10% of the chord length. It is not supposed to affect the transition as it doesn't provide a substantial change in the pressure gradient, which

might have altered the transition location. The span of the vane is $240mm$. The axial-chord c_x, *i.e.* the projection of the actual chord in the longitudinal direction (analogous to axial direction in case of a circular cascade) is $243mm$. The pitch l_p of the linear cascade, *i.e.* the clearance between the blades/vanes in transverse direction is $240mm$.

The control volume for the simulations is chosen as the volume enclosed by the pressure side of one blade and the suction side of the adjacent blade. The inlet and outlet sections are situated at distances greater than the chord length on either side of the leading and trailing edges. The lines joining the leading edges to the inlet section are based on the incident flow angle (mentioned later). Similarly, the ones joining the trailing edge to the outlet section are roughly based on slope of the camber line at the trailing edge; the choice is arbitrary.

4.2 Flow conditions and boundary specific restrictions

As per the design operation conditions, the angle of incidence of the flow is 25 degrees. The angle is defined with respect to the longitudinal direction of the *geometry-axes*. Reynolds number is calculated based on the axial-chord. Inlet flow conditions used in the experiments are depicted in Table 4.1. Other properties at the inlet were assumed to be ambient.

Inlet velocity	U_0	$20m/s$
Reynolds number	Re	3×10^5
Turbulent Intensity	I	3.5%
Turbulent length scale	l_s	0.0012

Table 4.1: Inlet flow conditions

B1	Inlet
B2	Outlet
B3 and B4	Periodic
B5 and B6	Walls
B7 amd B8	Periodic

Table 4.2: Boundary specifications

Figure 4.3 shows the flow domain with all the boundaries labelled as *B1* to *B8*. Table 4.2 elaborates the boundaries specific to each label in Figure 4.3. There is a

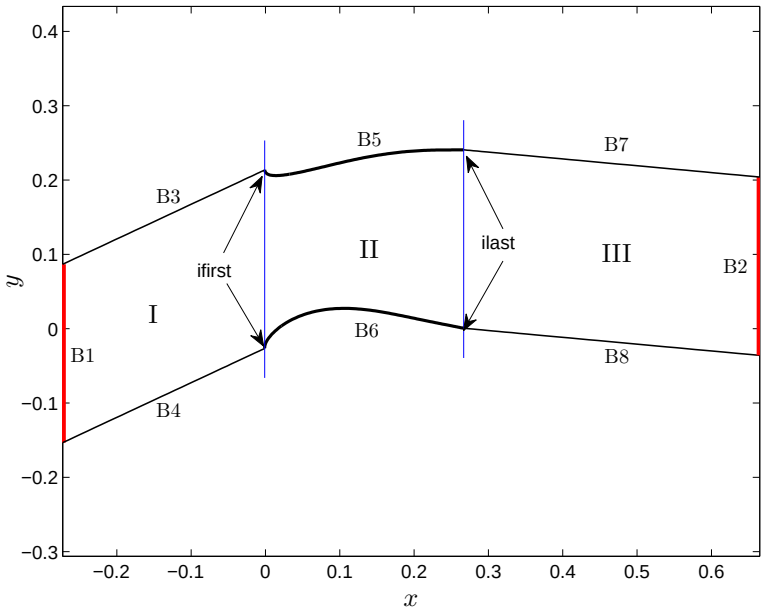

Figure 4.3: Control Volume containing the three sub-blocks I,II and III

certain restriction on the number of cells the mesh can have in each direction. This is imposed by the Multigrid method used to solve the pressure poisson equation (PPE), as explained in Chapter 3. Since the course mesh has a grid spacing which is twice as that of the fine one, the mesh should have cells equal to a multiple of 2^n in each direction, where n is the number of levels in the desired multigrid. The mesh under consideration, has another restriction though. The (i,j)-plane of the grid can be thought of as comprising of three sections/sub-blocks, separated by lines marked by the leading and trailing edge of the walls in the mesh i-direction (see Figure 4.3). *'ifirst'* and *'ilast'* represent the start and end of the walls respectively. These sections have different sets of boundary conditions in the j-direction. Section I and III are cyclic in j-direction, whereas section II has wall boundaries in j. While meshing, emphasis should be laid on the fact that in each section separately, number of cells in the i-direction should be a multiple of 2^n, where n is the desired number of levels.

4.3 Mesh generation

To generate the mesh, an in-house code is used called **G3DMESH**. The script can be found in Appendix A. The flow domain (in 2-D), as explained earlier, consists of three sections. These sections are blocked separately and then combined to a single block. This is done for two reasons: one, obviously for ease in meshing, and second, more importantly, to control the number of cells in each section in the i-direction. The generated mesh is two-dimensional with quad cells and later while running simulations, these 2-D layers are stacked in the third direction (spanwise) with suitable distance between them.

This gives rise to a three-dimensional single-block mesh ((i,j)-plane denoting the 2-D cross-sectional plane and k, the spanwise direction).

MESH	**ni(I)**	**ni(II)**	**ni(III)**	**nj**	**nk**	$\mathbf{z_{max}}$
MESH-1	40	128	40	112	32	$0.05144c_x$
MESH-2	40	128	40	112	64	$0.05144c_x$
MESH-3	40	128	40	112	128	$0.10288c_x$

Table 4.3: Mesh specifications – ni, nj, nk denote the number of cells in each direction; I, II and III denote the 3 sub-blocks; last column denotes the domain size in k-direction.

In the present study, the domain in k-direction (z_{max}) is chosen to be less than 20% of the chord-length (c_x), for achieving a good resolution for LES. Most of the study is done on a mesh with z_{max} equal to $0.05144c_x$ ($< 0.2c_x$). The three types of meshes to be used in the study are specified in Table 4.3.

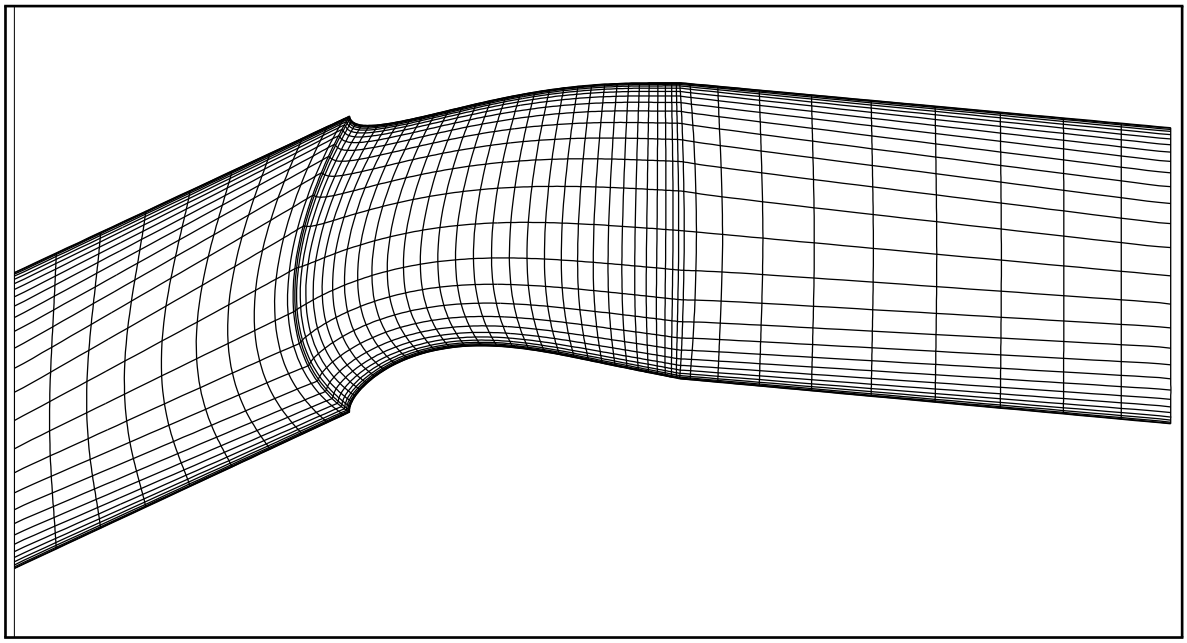

Figure 4.4: Complete mesh, made four times coarser for clarity

Figure 4.4 depicts the 2-D mesh corresponding the (i,j)-plane. For the sake of clarity, the mesh is made four times coarser in both directions. The resolution at the walls is similar to that used in the study by Collado Morata *et al.* [4]. Their mesh for structured

LES had resolution (in wall-plus units) at walls as: $\Delta x^+ \sim 150$, $\Delta z^+ \sim 25$ and $y^+ \sim 1$. In the present simulations based on the local wall friction velocity, Δx^+ is close to 150 mostly and goes up to 250 in the initial laminar region on suction side, $\Delta z^+ < 15$ and $y^+ < 1$. Δz^+ and y^+ also go a little higher than mentioned in the initial laminar region. The streamwise variation of these values can be found in the appendix B.

5

Case Set-up and Implementation

The simulations are carried out using CALC-LES, a cell-center based finite-volume in house code at the department. For space discretization, central-differencing scheme is used for all the velocity equations, whereas van-Leer scheme is used for the temperature equation. Crank-Nicolson method is used for temporal dicretization of all the equations. The numerical method explained by Davidson and Peng [45], is based on an implicit two-step time advancement technique with a multigrid pressure Poisson solver and a non-staggered grid system.

5.1 Boundary conditions

fluid properties		
Density	ρ	1
Prandtl no.	Pr	0.7
inlet conditions		
Inlet velocity	U_{in}	1
Reynolds no.	Re	3×10^5
Inlet Temperature	θ_{in}	0

Table 5.1: Flow conditions

The variables used in the simulation are all non-dimentional quantities. To compare the results with the experimental ones, the latter are then non-dimentionalized, generally using inlet velocity and axial chord c_x. Table 5.1 illustrates the fluid properties and inlet

flow conditions used for the simulation. The types of boundaries for the 2-D flow domain are explained in Chapter 4. Table 5.2 illustrates the various boundary conditions used in the simulation.

Inflow	Dirichlet(U_{in}, θ_{in})
	Neumann($\frac{\partial p}{\partial n} = 0$)
	Forced inlet fluctuations
Outflow	Convective BC for u, v, w
	Neumann for p, θ
Walls	No-slip(u=v=w=0)
	Constant heat flux ($q_w = 10$)

Table 5.2: Boundary conditions. u, v, and w denote x, y, z components of velocity respectively.

Inflow Boundary: To define the inflow boundary, fixed values of velocity and temperature are used (specified in Table 5.1) and a fluctuation field with zero mean is superimposed on it. Use of zero Neumann boundary condition for pressure is customary to the solving of the PPE – both at inlet and outlet. Velocity fluctuation field is based on the turbulence intensity and turbulent length-scales mentioned at the inlet. This will characterize the different scales of motion in the FST, which is crucial in triggering transition.

Inlet Fluctuations: For prescribing the inlet turbulence conditions at the inflow boundary, synthetic isotropic fluctuations are used. They are generated using the method specified by Davidson in [48]. It was found that the turbulence intensity specified at the inlet dropped considerably within a very short distance downstream, before adopting a more physical decay rate. The intensity at the inlet thus, had to be raised to a suitable value, so that the intensity at the leading edge is close to that mentioned in the experimental studies.The fact that larger length scales decay at a slower rate [49] provided motivaiton to use an integral scale larger than that reported in the experiments. Even in actual flows, a decay in turbulence is observed and turbulence evolution depends upon the origin of tubulence [49], which is not specified in the experiments corresponding the present studies. As stated by Ovchinnikov *et. al.* [49], for this reason, to match with the exact experimental data, it is important to know the turbulence characteristics, at least the integral length scale and the intensity, at the leading edge. These data are not provided in the experimental studies. The foremost aim is however not to mimic the transition location from experiments exactly. Rather, it is to observe transition first and then make changes in the inflow turbulence to match with the exact location

of transition. Table 5.3 depicts the turbulence specifications of both experiments and simulations.

experiments		
Turbulent Intensity	I	3.5%
Turbulent length scale	l_s	1.2×10^{-3} m
synthetic fluctuations		
Turbulent Intensity	I	10%
Integral length scale	l_s	4.8×10^{-3} m
Integral time scale	τ	2.1×10^{-3} s

Table 5.3: Inlet turbulence: experiments and simulations

WALLS: No slip boundary and constant heat flux is specified at the walls. q_w specified in Table 4.2 for the walls is the ratio of heat flux (q) to density (ρ) times isobaric heat capacity (c_p), $q_w = \frac{q}{\rho c_p}$. For pressure, zero Neumann condition is prescribed at the walls (as at inlet and outlet).

OUTFLOW BOUNDARY: At the outflow boundary, Convective boundary condition is used for describing velocity. If the outflow contains unsteadiness or vortical structures, it is important for the boundary condition to be specified in such a way that the vortices approach and pass the outflow boundary without much disturbance or reflection back into the domain. DNS or LES predictions are inherently unsteady and might contain dynamic vortical structures at the outflow. Moreover, in the present study the extent of the wake (which is dominated by such vortices) is unknown. Hence the presence of such unsteadiness is quite possible at the boundary. In such cases, when a non-reflective boundary condition is much demanded, *convective boundary condition* serves the purpose. It is defined as:

$$\frac{\partial \phi}{\partial t} + \bar{U}_n \frac{\partial \phi}{\partial x_n} = 0, \tag{5.1}$$

where x_n corresponds the coordinate in the mean flow direction and U_n corresponds the mean flow velocity. In the present case, U_n is taken as the bulk velocity based on the global mass influx.

5.2 Multigrid algorithm implementation

The current multigrid-code based on the Geometric Multigrid (GMG) method for Poisson equations was first implemented by Emvin for LES in a ventilated enclosure [50].

The FAS scheme discussed in the Chapter 4 along with the FMG scheme is employed in the code. The coarse grid assumes a grid spacing that is twice the fine grid in each direction. A coarse grid cell is obtained by merging eight fine grid cells into one. For both restriction and prolongation, linear projection is used. For smoothing, one of the several methods included in the code can be used. One is the normal 'symmetric point *Gasuss-Siedel* (GS) smoother', which is best suited for an isotropic mesh. The other one is using an 'alternating line GS smoother' (2D smoother), which has good smoothing properties for a stretched 2D grid. The third is an 'alternating plane relaxation GS smoother', wherein each (1,2)-plane is first solved exactly, followed by each (2,3)-plane and each (3,1)-plane. Here,1-2-3 directions are decided based on the mesh density in the different directions of the mesh. It is the most efficient method for meshes with high aspect ratio in a particular direction. More details on it can be found in [50].

5.2.1 Structure of the multigrid code

Flow-chart depicting the flow of information amongst the concerned subroutines in the CALC-LES code is shown in Figure 5.1. As mentioned earlier, the multigrid code is used for solving the pressure poisson equation (PPE). It is invoked at two regions in the solver. One in the subroutine *'main'* where it is initialized. The other in the subroutine *'calcpe'* where the PPE is solved.

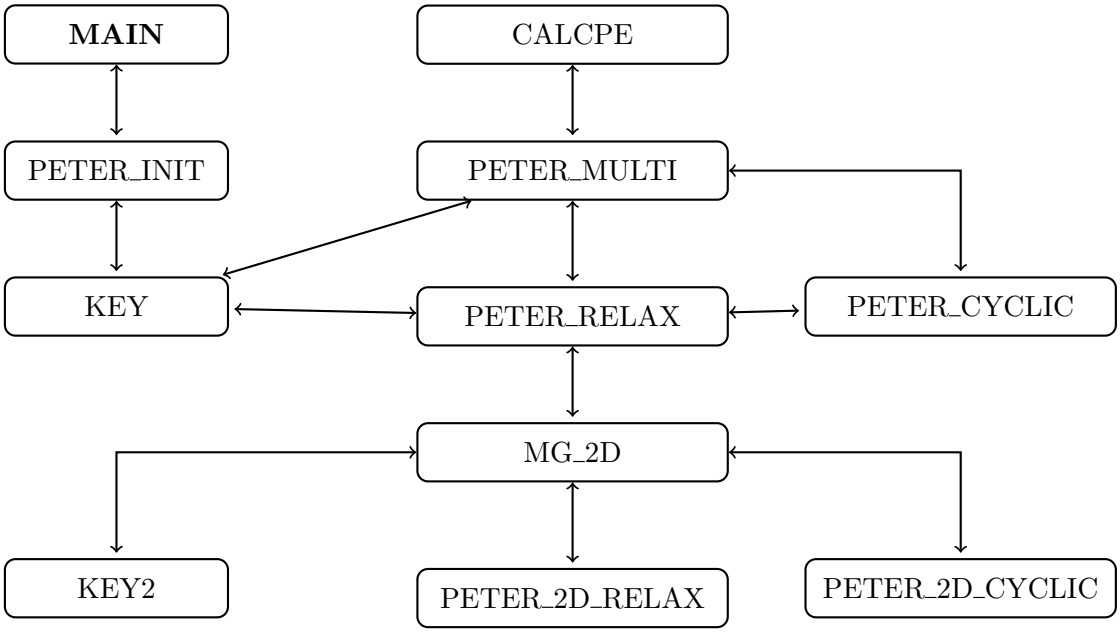

Figure 5.1: Flowchart of the multi-grid algorithm in CALC-BFC

Each of these subroutines are described below:

- **MAIN:** As mentioned above, the MG code is initialized in this subroutine by

calling *'peter_init'*. The arguments passed include information about the number of cells in each direction, their x, y and z coordinates, the logical constants for cyclic conditions in each direction, and the first and last cell number marking the extent of the walls in i-direction of the mesh-grid (region II in Figure 4.3).

- **PETER_INIT:** Based upon the restrictions described in Chapter 4, the grid is divided into required MG levels. Cells defining the extent of the wall in i-direction (*ifirst* and *ilast*) are identified. Subroutine *'key'* is called which helps storing the variables lexically into an array/list. This is done for all the MG levels. The coefficients for the PPE at all MG levels are computed. Then the cell aspect ratios are computed in all the directions, which decides the choice of the type of smoother, explained in the beginning of this section, to be used. In the end, boundary conditions at all the levels are specified. As has been the case throughout the code, the j-direction boundary condition for the current problem (part *cyclic* and part *wall* BC) is modified based on the location of the *ifirst* and *ilast* nodes, which differs at different MG grid-levels.

- **KEY:** As explained above, this subroutine helps in sorting the elements in a 3-D matrix based storage lexically into a pointer based array/list. The input arguments include the MG grid-level and the number of nodes in each direction for that level.

- **CALCPE:** This is the second instance in the CALC-LES code where the MG function is evoked, the first being *'main'*, where the MG code was initialized. It is here, that the PPE is solved. If the variable *multig* is set to true, then subroutine *'peter_multi'* is called.

- **PETER_MULTI:** The input/return arguments include the initial source term in the PPE (comprising of the velocity correction term), the pressure field, number of nodes in the three directions, total number of sweeps desired and the logical constants for cyclic conditions in each direction. First, with the help of the subroutine *'key'*, the source terms and the pressure field values are stored in a pointer based array at each MG level. The ones in the coarser level are initialized to zero.
  Next, a V(1,1)-cycle multigrid is performed without postsmoothing at the finest level. For that, a 'symmetric-point smoothing GS sweep' is performed starting at the finest level – first a forward smooth and then a backward one. Subroutine *'peter_cyclic'* is called to ensure cyclic conditions on the boundaries before and after each sweep. This corresponds to the first step of the FAS scheme – fine grid iterations – discussed earlier (Chapter 3).
  Then at the same MG level, *'peter_relax'* is called to solve the PPE. For the coarser levels, this corresponds to the third step of the FAS scheme – relaxation. Next, the source term is computed for the given MG level and it consists of the residual correction from the earlier relaxation step and the multigrid source (that is nothing but the restricted source term from the previous finer level).
  Following this, the source term at the next coarser level is computed, consummating the second step of the FAS scheme – restriction. It should be noted that

pressure is not exactly restricted similarly as explained earlier in the steps of FAS scheme. But instead, it is initialized to zero at the coarser levels. It is explained in more detail in [46].
The above procedure is followed regressively, until the coarsest level is reached. Restriction is not performed for the coarsest level. First leg of the V(1,1) cycle ends here. Starting at this level, the pressure field is interpolated to the next finer levels – prolongation. More information regarding the prolongation method can be found in [46]. This is followed by postsmoothing at each level leaving out the finest level.

- **PETER_RELAX:** This subroutine is invoked in *'peter_multi'* and it serves the purpose of the smoother or solver for the multigrid method. Based upon the aspect ratios computed in *'peter_init'*, the type of solver is decided. The first one is a 'symmetric point GS smoother', comprising of forward and backward sweeps.
The second type is an 'alternating-line GS smoother'. It has three subtypes, an 'X-line GS', a 'Y-line GS' and a 'Z-line GS' smoother, with smoothing performed along grid lines corresponding to that line GS.
The third is an 'alternating-plane GS smoother'. It also has three subtypes depending upon the chosen plane of smoothing, 'X-plane', 'Y-plane' and 'Z-plane' GS smoother, the prefix indicating the normal direction of the chosen plane. For example, X-plane GS smoother means that all the planes corresponding the (j,k)-directions of the grid are relaxed one by one. This is performed by calling the subroutine *'mg_2d'*. A logical variable 'wallj' is defined to maintain discrepancy in passing arguments to *'mg_2d'* regarding the kind of boundaries possessed by that particular (j,k)-plane of the grid. In the present case, while performing X-plane GS smoothing, some (i,j)-planes have cyclic boundary condition in the j-direction and some have wall or no-slip boundary condition.
After one of these smoothing operations is performed, *'peter_cyclic'* is called to ensure cyclic boundary conditions when appropriate.

- **MG_2D:** This subroutine performs a 2D multigrid operation on the given plane passed as input argument and is similar to the 3D multigrid operation performed by *'peter_multi'*. The input/return arguments to this subroutine include the coefficients and the source terms of the equation pertaining to the concerned plane, the logical variables related to cyclic boundaries, variables denoting the overall 3D MG level and the choice of plane-smoother (X,Y or Z), cell number defining the extent of wall in that direction for that MG level (related to ifirst and ilast), and the logical variable discussed earlier, 'wallj'.
It uses another subroutine *'key2'* to store the initial source term in a lexically converted pointer based array. Subroutine *'peter_2d_cyclic'* is called to ensure correct boundary conditions. Once the coarsest 3D MG level is reached, this subroutine performs a 2D relaxation on the planes pertaining to that MG level and returns the pressure field.
For all the other intermediate levels, it performs a V(1,1)-cycle 2D multigrid. It

starts with 2D-plane relaxation at the given level, which is performed by calling the subroutine *'peter_2d_relax'* and the source term is computed at that level.
Next, the source terms are restricted to the next coarser level and the coefficients are computed at the same level. Pressure at the coarser level is initialized to zero as in *'peter_multi'*.
Once the coarsest level in 2D multigrid is reached, the pressure is prolongated to the next finer level, followed by relaxation at that level by calling *'peter_2d_relax'*. Relaxation is not performed on the finest level though, and the pressure field over the 2D plane is returned to *'peter_relax'*.

- **KEY2:** This is similar to the subroutine *'key'*. It creates pointer based storage of variables from a 2D matrix based storage. The input arguments include the variable indicating the MG level and the maximum number of nodes in each direction.

- **PETER_2D_RELAX:** This subroutine performs relaxation on the 2D plane passed as input argument by *'mg_2d'*. It has the same input arguments as for *'mg_2d'*, and in addition to it, the number of iteration sweeps to be performed as well. Based upon the choice of smoother (X, Y or Z-plane GS) and the type of boundaries (periodic or not), it performs a TDMA operation to solve the pressure field (cyclic TDMA in case of periodic boundaries).

- **PETER_CYCLIC:** This subroutine is called in *'peter_multi'* and *'peter_relax'*, to enforce periodic boundary conditions at the required boundaries.

- **PETER_2D_CYCLIC:** It is similar in function to *'peter_cyclic'*. It enforces periodic conditions at required boundaries after performing 2D-multigrid in *'mg_2d'*.

6

Results and Discussion

6.1 Post processing of results

The simulations are run for an ample amount of time, 7 to 10 through-flow times (c_x/U_0), before sampling is started. It is enough to ensure that a statistically steady state is achieved. The averaging is then done for a time equivalent to 7 to 10 times of c_x/U_0. Pressure distribution over the guide vane and heat transfer at the guide vane walls are expressed by computing pressure coefficient, C_p and Nusselt number, Nu, at the walls respectively. C_p is computed as:

$$C_p = \frac{p - p_0}{\frac{1}{2}\rho(U_0)^2}, \tag{6.1}$$

where, p denotes the pressure where C_p is computed, p_0 and U_0 are the reference pressure and velocity, respectively, at the inlet of the domain, and ρ is the density of the fluid. Nu is computed as follows:

$$Nu = \frac{h}{k}c_x \tag{6.2}$$

$$= \frac{q/(\theta_w - \theta_\infty)}{\nu(\rho c_p)/Pr}c_x, \tag{6.3}$$

where, h and k are the convective heat transfer coefficient and thermal conductivity of the fluid respectively, c_x is the axial chord of the guide vane, θ_w and θ_∞ are temperature at the wall and in the free-stream (same as at inlet) respectively, ν is the kinematic viscosity, Pr is the Prandtl number, and q is the heat flux at the walls.

6.2 Comparison with the experiments

In this section, results from the experimental study ([7]) are compared with those from the simulations. As mentioned earlier, simulations are carried out using two differ-

ent SGS modelling techniques, 'smagorinsky' and 'dynamic SGS'. The residual statistics can be found in the Appendix.

6.2.1 Pressure distribution

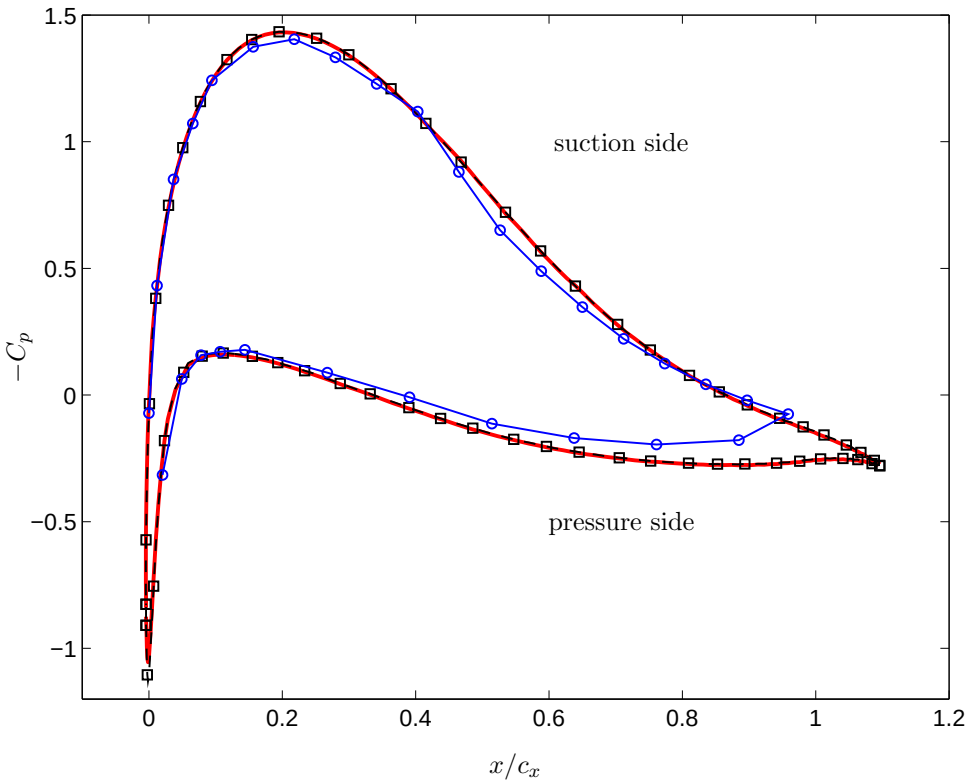

Figure 6.1: Coefficient of pressure at walls; –○– Experimental; — Dynamic-SGS; -□- Smagorinsky.

Figure 6.1 depicts the coefficient of pressure, C_p, distribution over the OGV. The x-coordinates are scaled with respect to the axial chord c_x. The experimental data were collected over the mid-span of the OGV. It can be seen that both the models (Smagorinsky and dynamic-SGS) are in good agreement with the experimental data qualitatively. The upper curve represents the suction side, characterized by a low C_p and the lower one, the pressure side, characterized by a higher C_p. $C_p \approx 1$ represents the stagnation point, which lies at the immediate vicinity of the leading edge on the pressure surface as reported in the experiments [7]. Though its exact location in simulations and experiment shows a very little discrepancy, that can be attributed to the lack of pressure measurement stations in experiments as compared to simulations (grid points), and can be ignored.

The initial accelerating part on the pressure side (approximately, $x/c_x = 0$ to 0.1)

is in very good agreement with the experiments. But then, from $x/c_x = 0.1$ onwards, the simulations show a higher deceleration as compared to the experiments. This can be attributed to the fact that in simulations the trailing edge is modified a little bit as discussed in Chapter 4. Also, there is a slight acceleration observed in the experiments after approximately, $x/c_x = 0.8$, that is absent in simulations. Both these observations can be attributed to the change in curvature and length of the trailing edge and hence, slight changes in the flow conditions downstream of it.

On the suction side, the local flow follows the trend shown by the experiments, accelerating till the throat of the cascade, approximately at $x/c_x = 0.22$, though the simulations show a slight higher acceleration. Further downstream, there is deceleration in the local flow. A distinct bump at $x/c_x = 0.4$ on the suction surface is observed in the experiments, which marks the onset of the boundary layer transition to turbulence. It is reported in the experimental study that this fact is corroborated by the presence of a transitional separation bubble at this point shown by the numerical analysis performed by the authors [7]. However, no such bump or separation bubble is observed in the

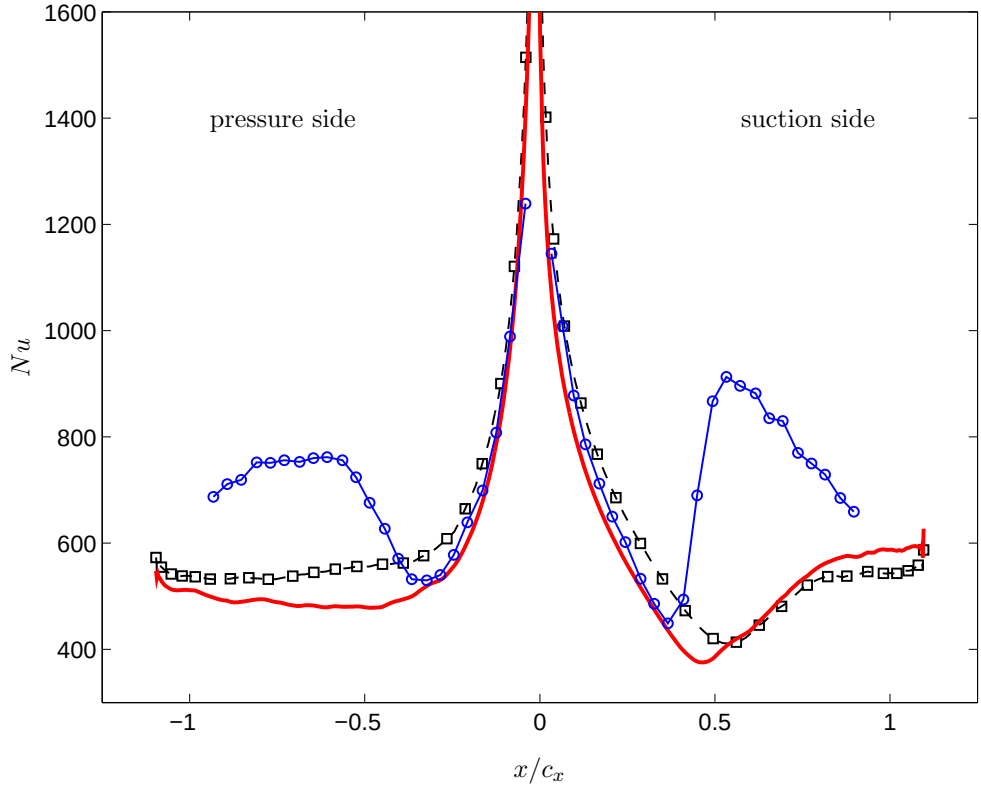

Figure 6.2: Nusselt number profile; –○– Experimental; — Dynamic-SGS; -□- Smagorinsky.

present analysis, showing a more smoother pressure profile. The discrepancy at the trailing edge is again expected due to the modification of the trailing edge in the present

simulations as discussed earlier. Also, it can be observed that both Smagorinsky and Dynamic-SGS model predict a similar pressure distribution over the OGV. The overall shape of the pressure coefficient profile in the simulations suggests that the local flow over the OGV is forced to remain laminar.

6.2.2 Heat transfer distribution

To investigate the boundary layer transition further, heat transfer analysis is performed. As in the experiments, Nusselt number (Nu) profile over the OGV surface is studied, as can be seen in figure 6.2. The x-coordinates on the pressure side are represented on the negative x-axis. It can be seen from the figure that the profiles of Nusselt number (Nu) from simulations are not matching with the experimental data. At the leading edge, Nu is very high owing to the smaller width of laminar boundary layer there. The very high values of Nu are clipped in the plot, since they are of very little importance to the present study. As the flow accelerates on both the sides from the stagnation point, the boundary layer thickness increases, and the value of Nu drops as the boundary layer grows. Thereafter, further downstream, as reported in the experiments, there is a sharp increase in Nu, starting at around $x/c_x = -0.32$ on the pressure side and at $x/c_x = 0.36$ on the suction side, indicating the onset of transition to turbulence. This trend is not found in the simulations performed, indicating that the boundary layer is still remaining laminar.

On the pressure side, further downstream of $x/c_x = -0.32$, where the experiments showed a significant increase in Nu, the simulations on the other hand follow the prevailing decreasing trend in Nu and then get fairly constant towards the trailing edge. Smagorinsky model constantly predicts a slightly higher value than dyanmic-SGS in this region. On the suction side though, further downstream of $x/c_x = 0.36$ (onset of transition predicted by experiments), at around $x/c_x = 0.45$ in case of dynamic-SGS and $x/c_x = 0.56$ in Smagorinsky case, the Nu number shows a gradual increase. This rise is different from that observed in experiments, both the magnitude and the rate of growth being too low or small as compared to the experiments. Moreover, the physical trend of transition, shown by a sudden increase first, evident of transition, followed by a gradual decrease that testifies an expanding (turbulent) boundary layer, cannot be observed in the present simulations. Detailed analysis of the boundary layer will be done in the upcoming sections.

6.3 Mesh independence study

As mentioned in Chapter 4, three types of meshes are studied (see Table 4.3). MESH-2 has a better spanwise resolution than MESH-1, and MESH-3 has the same spanwise resolution as MESH-2, but it has more number of sample nodes than MESH-2 (twice). Figure 6.3 depicts the C_p and Nu profile over the guidevane surface for these meshes. It can be seen that the pressure curve overlaps completely in all the three cases. The

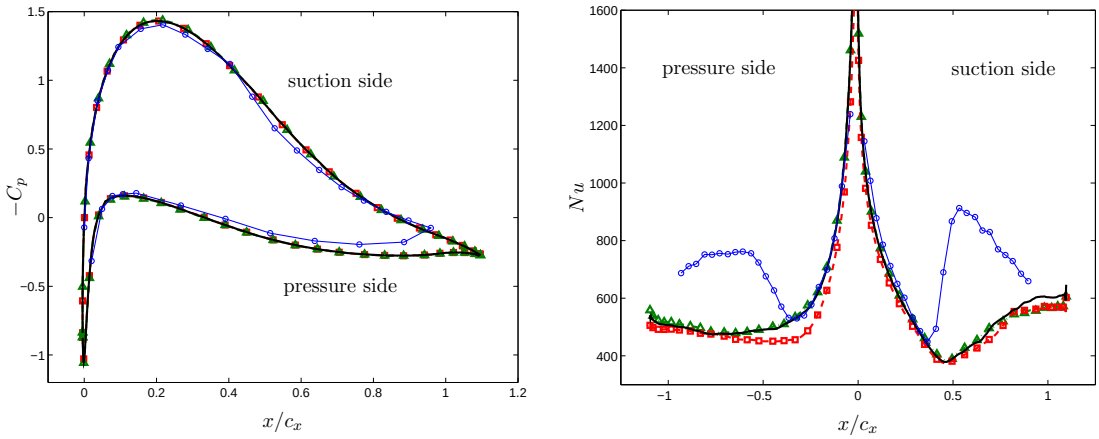

(a) Coefficient of Pressure, C_p **(b)** Nusselt number, Nu

Figure 6.3: –○– Experimental; — MESH-2 ($nk = 64$, $z\,|_{max}= 0.0125$); -□- MESH-1 ($nk = 32$, $z\,|_{max}= 0.0125$); -△- MESH-3 ($nk = 128$, $z\,|_{max}= 0.025$).

heat transfer profile for MESH-2 and MESH-3 are very close, since they have the same resolution. But they have different spanwise domain size, which shows that the spanwise domain has no significant effect on the transition. It can also be said that the spanwise resolution does not play an important role in the present simulations, since MESH-1 and MESH-3 give very similar results.

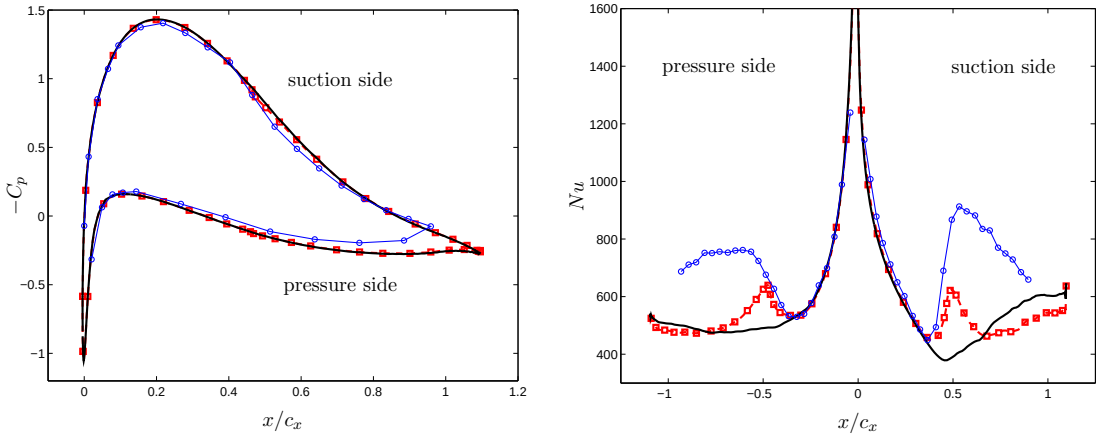

(a) Coefficient of Pressure, C_p **(b)** Nusselt number, Nu

Figure 6.4: –○– Experimental; — MESH-2 ($nk = 64$, $z\,|_{max}= 0.0125$); -□- MESH-2B (same as MESH-2, refined in streamwise direction in the transition zone).

A separate set of simulations were performed on a mesh with same number of cells as in MESH-2, but with streamwise resolution refined in the transition zone. It will be referred to as MESH-2B. Figure 6.4 depicts the C_p and Nu profile over the guidevane surface for these meshes. It can be observed that in the simulations with MESH-2B,

the Nu profile follows the experimental curve very closely for a very short distance in the transition zone on both suction and pressure sides. It shows an initial increase for a while, but then drops down in the middle of the transition zone. The momentary increase

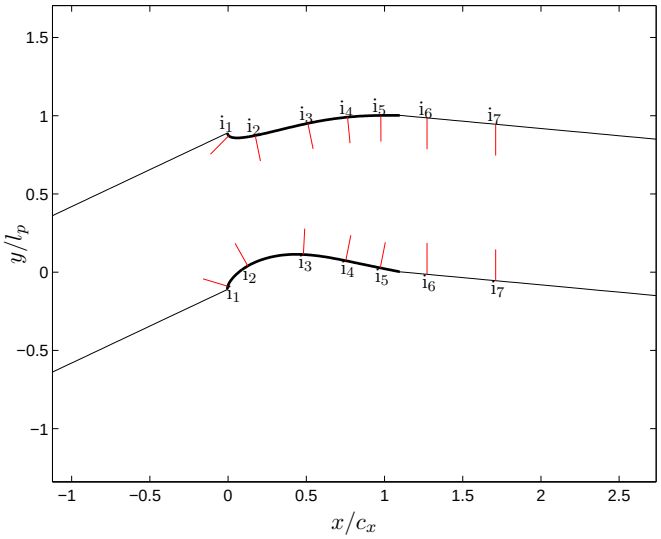

Figure 6.5: stations for study of stresses and fluxes

indicates that the non-linear interactions in the boundary layer have been triggered. But then, once triggered, it should have continued to grow. It could be possible that a very fine streamwise resolution is needed for the non-linear interactions to be sustained continuously.

6.4 Boundary layer study

It becomes imperative now to understand the flow in the boundary, so as to understand why the simulations do not comply with experiments. In this section also, results from both Smagorinsky and dynamic-SGS model are presented. All the results in this section pertain to the simulations carried out on MESH-2. Resolved Reynolds stresses and heat fluxes are plotted at certain stations on the cascade surfaces and in the wake region downstream of trailing edge. Figure 6.5 depicts the location of all the stations. All the variables plotted at these stations over the surface are transformed to the local coordinate system corresponding to the wall with one axis parallel to the wall in the streamwise direction (subscript 's') and the other normal to the wall pointing into the domain (subscript 'n'). The third axis (subscript 'z') is parallel to the spanwise direction in the global coordinate system. The stresses and fluxes will be plotted with respect to the normal distance from wall (Δn) scaled by the pitch of the cascade (l_p). A second axis is also shown most of the time depicting the y^+ values corresponding the normal distance. Also, plotted are the maximum *rms* velocity and temperature profiles over the surface.

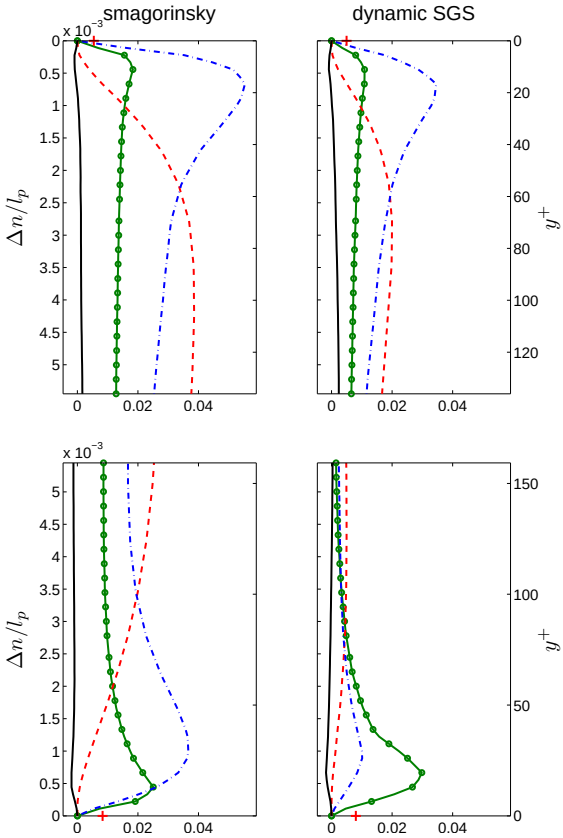

Figure 6.6: Stresses at i_1; top: pressure side ($x/c_x = 0.004$), bottom: suction side ($x/c_x = -0.002$). Legends: -o-$\langle v_s' v_s' \rangle$; - -$\langle v_n' v_n' \rangle$; -·-$\langle v_z' v_z' \rangle$; —$\langle v_s' v_n' \rangle$; +wall shear stress.

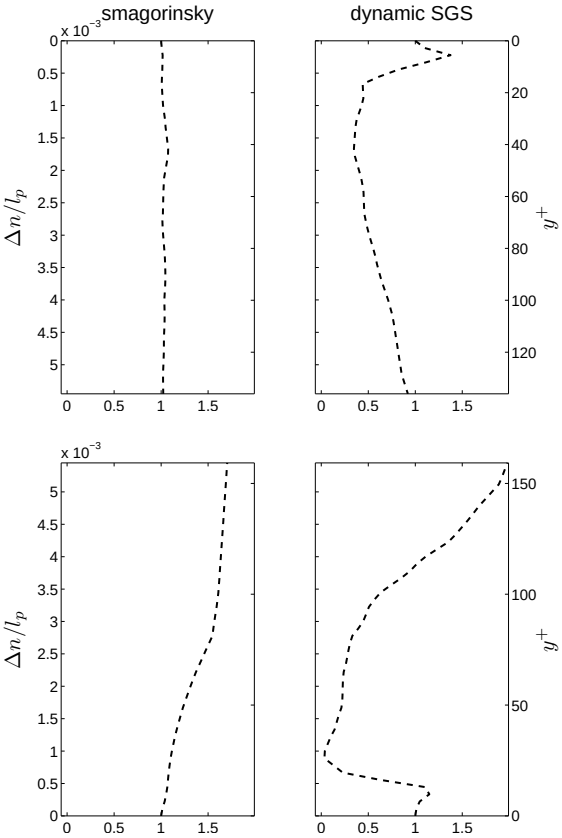

Figure 6.7: Total viscosity at i_1; top: pressure side ($x/c_x = 0.004$), bottom: suction side ($x/c_x = -0.002$). Legends:- -ν_{tot}/ν

6.4.1 Resolved stresses

Figure 6.6 illustrates the stress values at station i_1, the top row corresponding the pressure side and bottom, the suction side. The local wall shear stress at that location is also depicted ('+' marker on the x-axis). Figure 6.7 depicts the total viscosity ($\nu_{tot} = \nu + \nu_r$) scaled by kinematic viscosity (ν) at the points corresponding to those in the Figure 6.6. It can be seen in Figure 6.6 that with both the models, normal stress on the pressure side in the spanwise direction, $\langle v_z' v_z' \rangle$ is largest. This shows that this point is close to the stagnation point discussed in the previous section. On both sides, the wall normal component $\langle v_n' v_n' \rangle$ of the stress is negligible very close to the wall. In the dynamic-SGS simulation, negative values of ν_r can be seen near the walls ($\nu_{tot}/\nu < 1$), indicating the presence of backscatter, but contrarily the stresses seem to be more damped than in the Smagorinsky case.

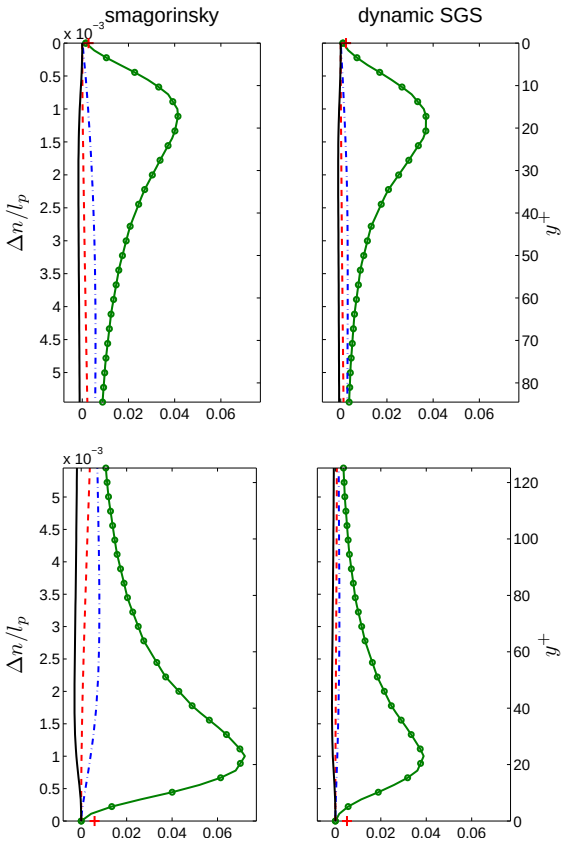

Figure 6.8: Stresses at i_2; top: pressure side ($x/c_x = 0.174$), bottom: suction side ($x/c_x = 0.126$). Legends: as in Figure 6.6

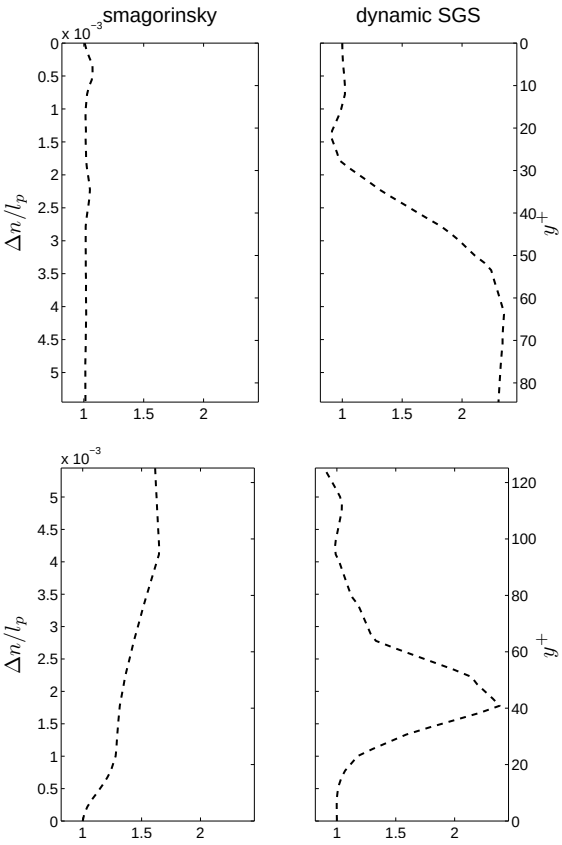

Figure 6.9: Total viscosity at i_2; top: pressure side ($x/c_x = 0.174$), bottom: suction side ($x/c_x = 0.126$). Legends: as in Figure 6.7

Figure 6.8 and Figure 6.9 represent the stresses and total viscosity at station i_2. This station lies in the locally accelerating part of the domain. It can be seen that the streamwise component of stress $\langle v_s' v_s' \rangle$ is the most dominating part and the other components are negligible. This observation is more prominent in the dynamic-SGS simulation, probably due to the higher residual viscosity predicted by it (Figure 6.9). This region of the boundary layer is probably laminar in nature.

In Figure 6.10 shows the stresses at station i_3. It can be seen that $\langle v_s' v_s' \rangle$ is still very large as compared to the other components. On the suction side, it has increased almost 1.5 times of its value near the wall at section i_2 (Figure 6.8). Also, it can be seen the boundary layer thickness has increased considerably, as this streamwise component is much bigger than the corresponding value at section i_2 even farther away

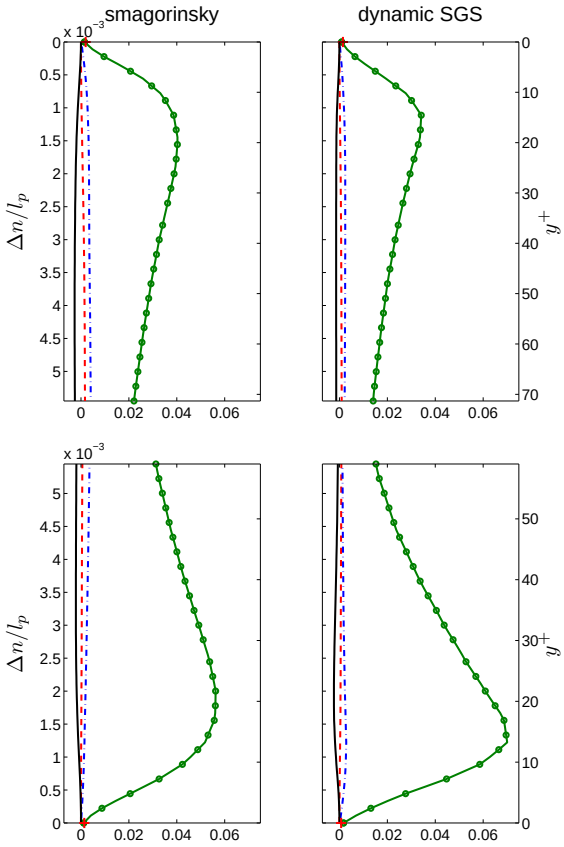

Figure 6.10: Stresses at i_3; top: pressure side ($x/c_x = 0.510$), bottom: suction side ($x/c_x = 0.482$). Legends: as in Figure 6.6

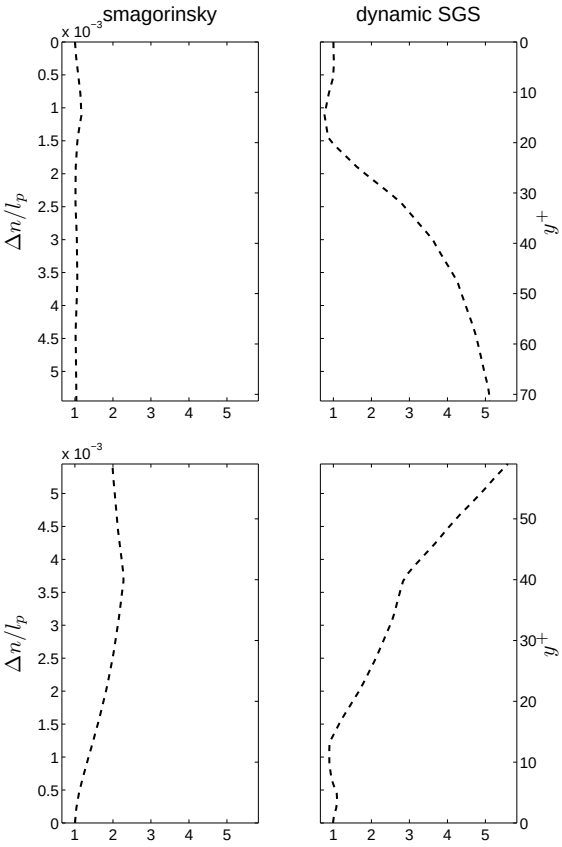

Figure 6.11: Total viscosity at i_3; top: pressure side ($x/c_x = 0.510$), bottom: suction side ($x/c_x = 0.482$). Legends: as in Figure 6.7

from the wall. This can be seen on both suction and pressure side walls. Moreover, the lower y^+ values show that the wall friction velocity has decreased from earlier, which is obvious as the local flow is decelerating. This is supported further by the very low value of wall shear stress (a '+' marker on the x-axis in the figure). Now, according to the experiments (section 6.2), at this station, the boundary layer is on the verge of attaining full turbulence. This implies that the other components, namely wall-normal (n direction) and spanwise (z direction), should have increased significantly. It can be inferred that in the present simulations, the non-linear interactions responsible for distribution of stresses in different directions are absent. This will be discussed further in upcoming sections.

Figure 6.12 represents the stresses at station i_4. Here, as per the experiments, the boundary layer should have gone completely turbulent. That means an isotropic dis-

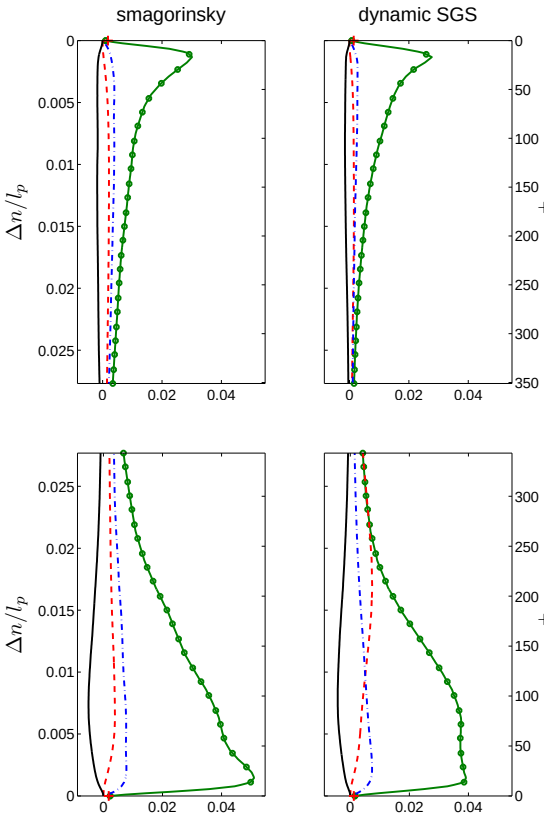

Figure 6.12: Stresses at i_4; top: pressure side ($x/c_x = 0.764$), bottom: suction side ($x/c_x = 0.752$). Legends: as in Figure 6.6

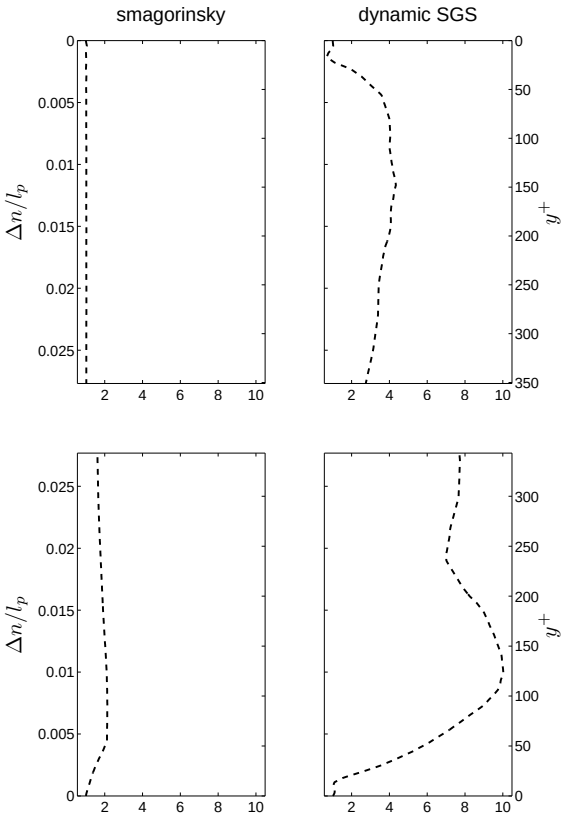

Figure 6.13: Total viscosity at i_4; top: pressure side ($x/c_x = 0.764$), bottom: suction side ($x/c_x = 0.752$). Legends: as in Figure 6.7

tribution of stresses in all directions except for the wall-normal component close to the wall. This is not found in the present simulations. On the suction side though, the spanwise component $\langle v_z' v_z' \rangle$ shows a slight increase close to the wall and the wall-normal component $\langle v_n' v_n' \rangle$ little away from the wall, both compared to their corresponding values at station i_3 (Figure 6.10). The pressure side too shows a similar increment, but very small in magnitude. The suction side clearly shows signs of growing turbulence, as emphasized by the Nusselt number plot in figure 6.2.

Further downstream, at station i_5, the stresses are depicted in figure 6.14. This is almost the trailing edge of the OGV, and here the geometry is different from the one in experiments, as mentioned earlier. Here, the boundary layer thickness has increased considerably both on suction and pressure sides. On the suction side as in the previous station, i_4, $\langle v_n' v_n' \rangle$ and $\langle v_z' v_z' \rangle$ are significant.

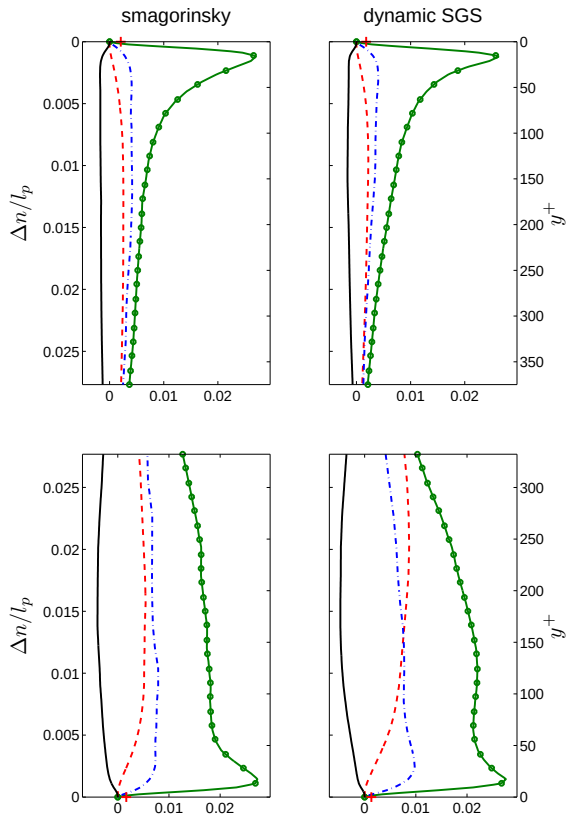

Figure 6.14: Stresses at i_5; top: pressure side ($x/c_x = 0.976$), bottom: suction side ($x/c_x = 0.973$). Legends: as in Figure 6.6

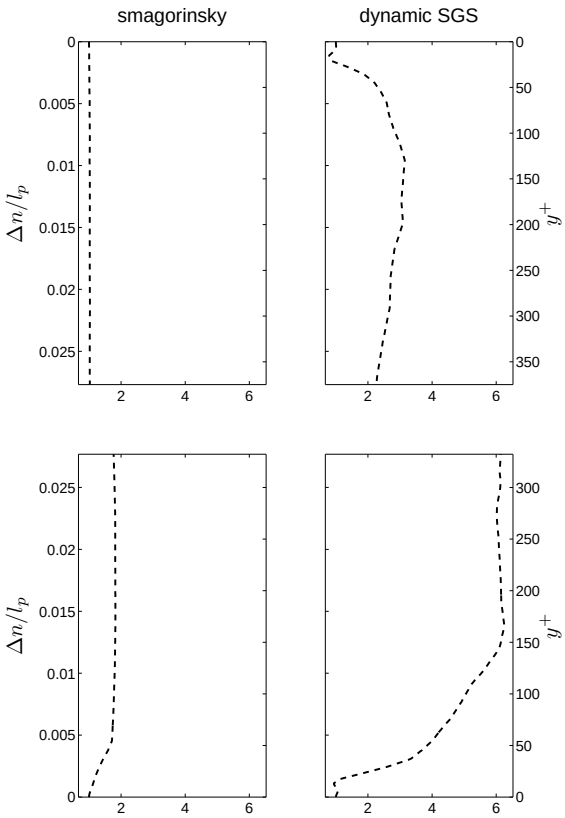

Figure 6.15: Total viscosity at i_5; top: pressure side ($x/c_x = 0.976$), bottom: suction side ($x/c_x = 0.973$). Legends: as in Figure 6.7

Stations i_6 and i_7 correspond to the wake region. Here, the stress components are plotted in the global coordinate system as there is no wall. Δn on the y-axis corresponds to the distance from the corresponding domain boundaries. Figure 6.16 depicts stresses at i_6. The two shear layers from the suction and pressure surface merge in this region, resulting in the formation of large scale vortices, which enhance the turbulence. This region, called the wake, keeps on expanding in space, as can be seen in figure 6.18. It can be seen that the disturbance is felt further away from the domain boundary at this station; meaning, the wake region is expanding. Moreover, it can also be seen that the SGS viscosity goes very high in this region as compared to the earlier stations. This can be expected since the mesh is quite coarser here, and only the very large scale eddies are being resolved. The present study does not delve into the analysis of this wake region.

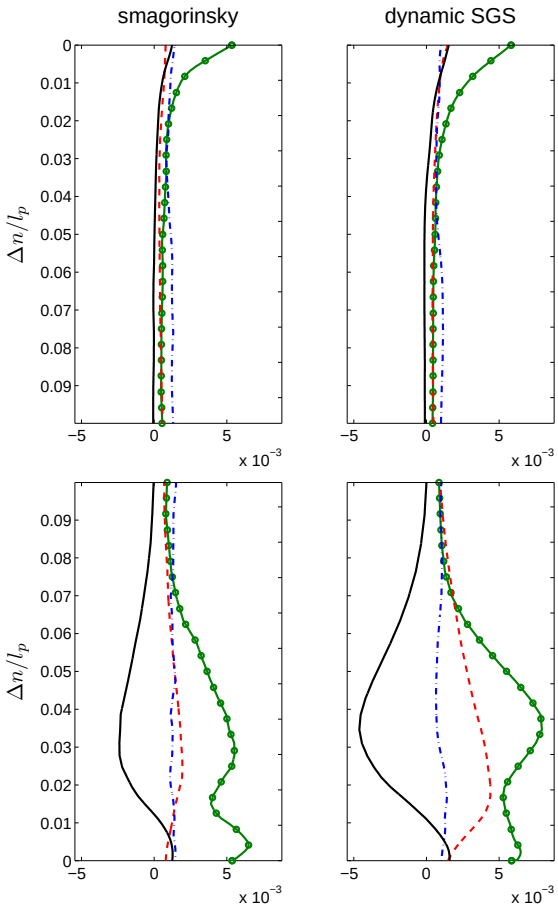

Figure 6.16: Stresses at i_6; top: pressure side ($x/c_x = 1.272$), bottom: suction side ($x/c_x = 1.272$). Legends: $-\circ-\langle v'_x v'_x \rangle$; $--\langle v'_y v'_y \rangle$; $-\cdot-\langle v'_z v'_z \rangle$; $—\langle v'_x v'_y \rangle$.

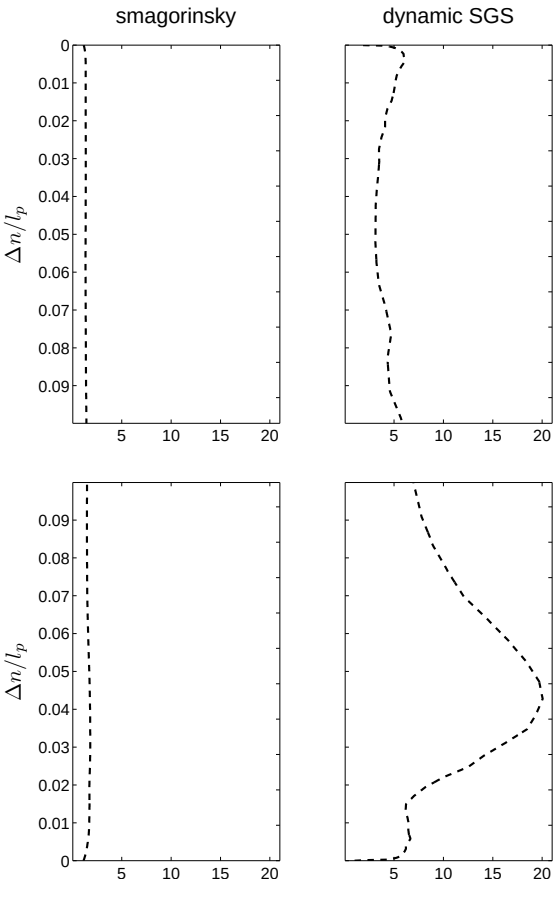

Figure 6.17: Total viscosity at i_6; top: pressure side ($x/c_x = 1.272$), bottom: suction side ($x/c_x = 1.272$). Legends: as in Figure 6.7

Summing up the analysis of Reynolds stresses in the boundary layer, it can be said that there is a definite increase in the streamwise stress component as the flow moves downstream, while the same cannot be said for the wall-normal and spanwise components though. Both the models (Smagorinsky and dynamic-SGS), predict similar behaviour. The difference is not much, since the SGS viscosity is very small (as predicted by both the models) in the region of interest (close to the wall). The growth in the streamwise component, whether to be attributed to the free-stream fluctuations or artificial (non-physical) fluctuations caused by the central differencing (CD) scheme has to be investigated. CD scheme is generally used in LES for turbulent flows, since it is non-dissipative [51]. As a result, the numerical oscillations created this way help in sustaining turbulence and not dampen out. But, whether they aid in transition from (orderly) laminar to turbulent is not certain. In other words, if they can act as sources of disturbance, as provided

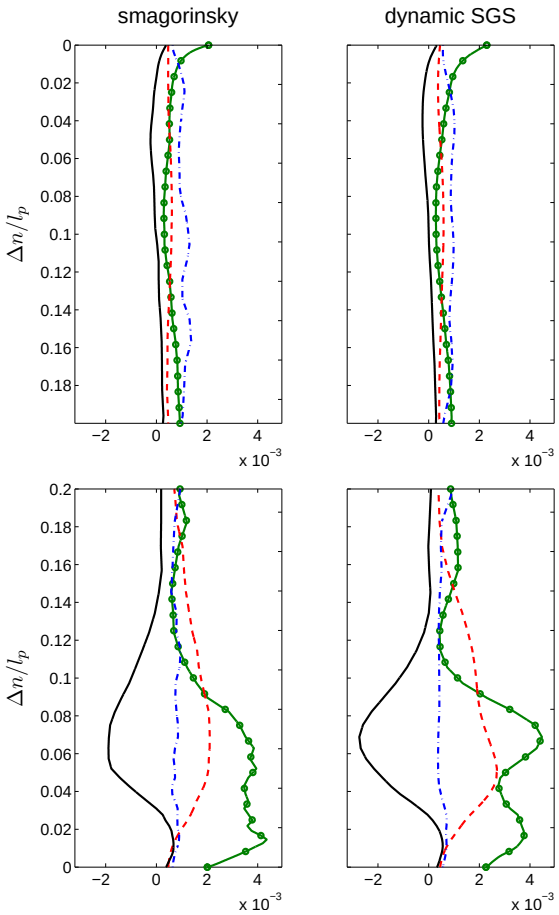

Figure 6.18: Stresses at i_7; top: pressure side ($x/c_x = 1.711$), bottom: suction side ($x/c_x = 1.711$). Legends: as in Figure 6.16

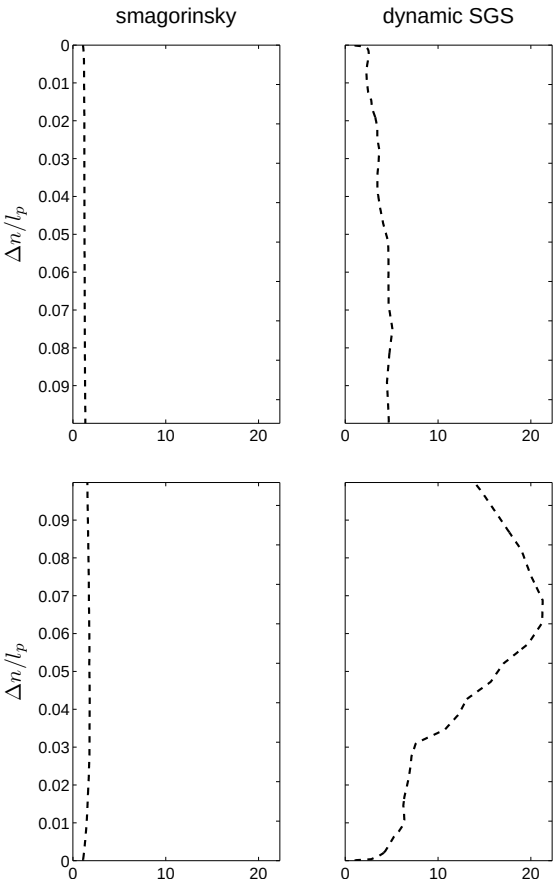

Figure 6.19: Total viscosity at i_7; top: pressure side ($x/c_x = 1.711$), bottom: suction side ($x/c_x = 1.711$). Legends: as in Figure 6.7

by FST, and invoke the non-linear modes is not known. Most certainly, they cannot; transition is very selective to FST scales (as discussed in chapter 2) and that cannot be provided by artificial oscillations (through CD scheme or otherwise). Nevertheless, CD scheme is always preferable due to its non-dissipative nature.

6.4.2 Momentum and thermal fluxes

In this section, the resolved part of turbulent momentum flux in wall normal direction, given by the Reynolds shear stress, $\langle v_n' v_s' \rangle$, and the thermal flux in the same direction, $\langle v_n' \theta' \rangle$, ($\theta$ denotes the temperature) are compared along with the molecular heat flux, $\left(\frac{\nu}{Pr} \frac{\partial \langle \theta \rangle}{\partial n} \right)$. This can give an idea about the penetration of wall-normal disturbances into the boundary layer. Here subscripts 's' and 'n' denote the wall-parallel

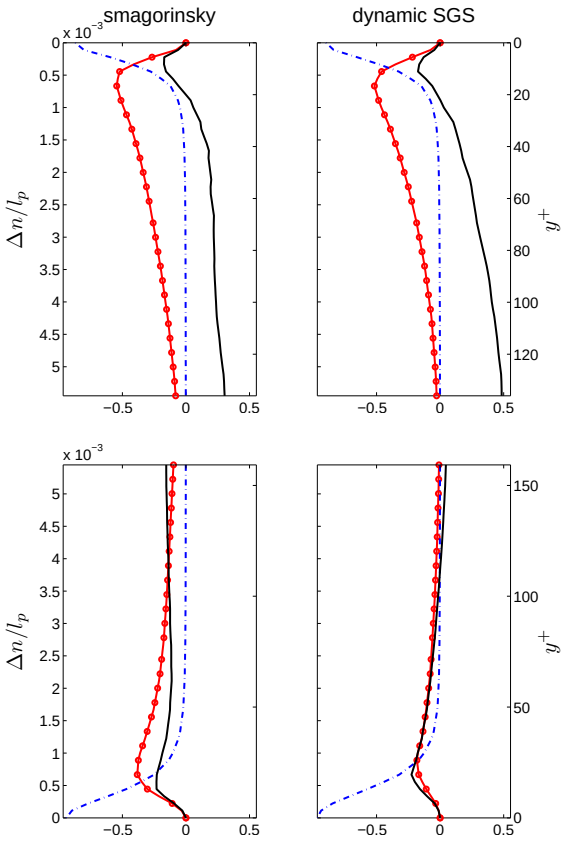

Figure 6.20: Fluxes at i_1; top: pressure side ($x/c_x = 0.004$), bottom: suction side ($x/c_x = -0.002$). Legends: —$\langle v_s' v_n' \rangle / \tau_w$; -○-$\langle -v_n' \theta' \rangle / q_w$; -·-$\left(\frac{\nu}{Pr} \frac{\partial \langle \theta \rangle}{\partial n} \right) / q_w$.

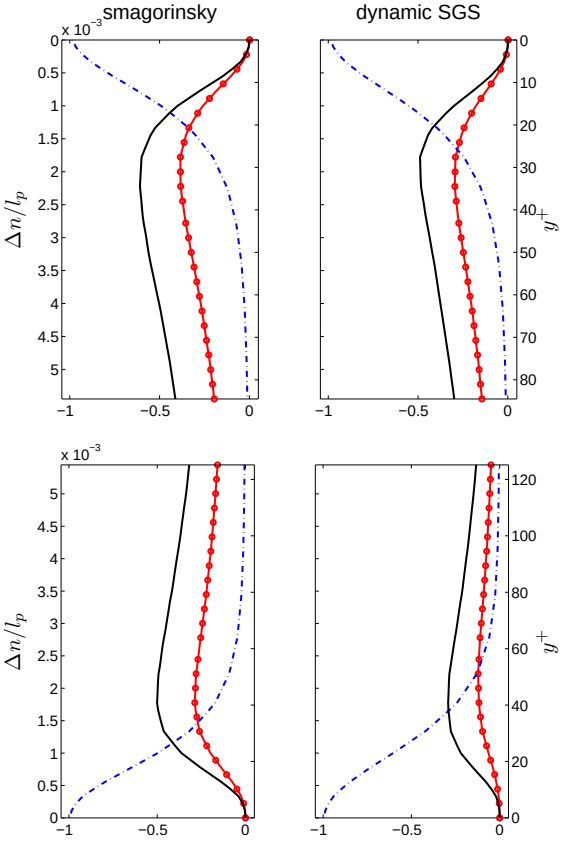

Figure 6.21: Fluxes at i_2; top: pressure side ($x/c_x = 0.174$), bottom: suction side ($x/c_x = 0.126$). Legends: same as in Figure 6.20.

and normal directions respectively. Due to the similar nature of the non-dimensionalized momentum and thermal equations, the turbulent flux terms mentioned will behave in the same way, in magnitude at least. On a flat plate with zero pressure gradient and unit turbulent Prandtl number (Pr_t), they are supposed to be equal in magnitude. They are of opposite signs if the plate is hotter than the fluid, as a result of the opposite nature of velocity and temperature gradients at the wall. A different discretization scheme for one of the variables (see beginning of Chapter 5) might also result in a difference, owing to numerical dissipation as a result of the particular discretization scheme. The momentum flux is normalized by the local wall shear stress τ_w, and the thermal fluxes are normalized by the local wall heat flux, which in the present case is a fixed value q_w throughout the surface.

Figure 6.20 depicts the fluxes at the station i_1. On the suction side, the turbulent

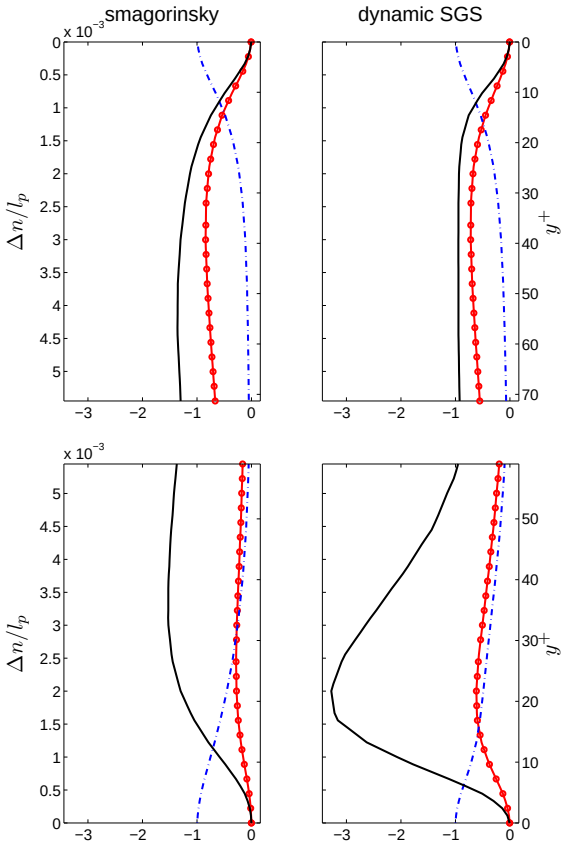

Figure 6.22: Fluxes at i_3; top: pressure side ($x/c_x = 0.510$), bottom: suction side ($x/c_x = 0.482$). Legends: same as in Figure 6.20.

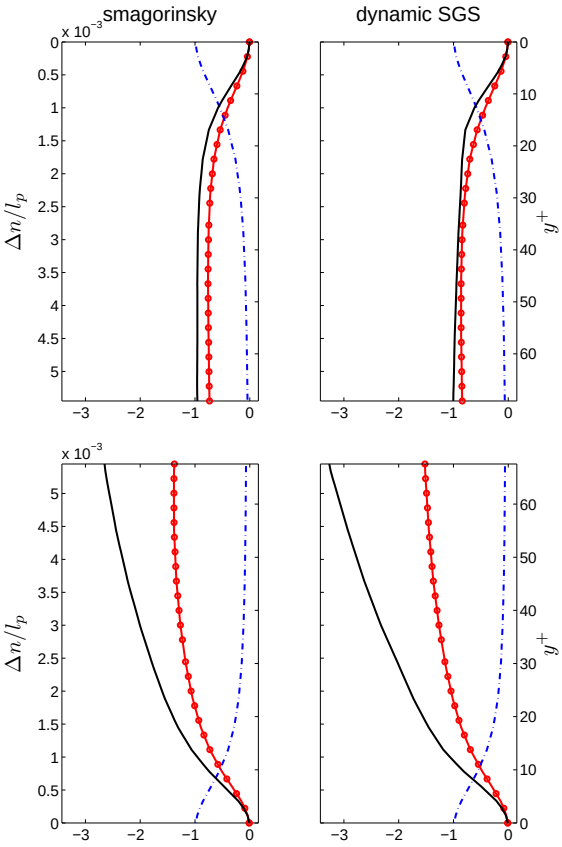

Figure 6.23: Fluxes at i_4; top: pressure side ($x/c_x = 0.764$), bottom: suction side ($x/c_x = 0.752$). Legends: same as in Figure 6.20.

momentum and thermal fluxes are almost identical. Comparing Figure 6.20 and Figure 6.21, it can be seen that the thermal boundary layer is getting thicker downstream. Turbulent heat flux is lower at all stations inside the boundary layer as compared to the molecular/viscous one. From the transport equation of the wall-normal heat flux vector $v_2'\theta'$, assuming the streamwise temperature gradient ($\frac{\partial\theta}{\partial x_1}$) to be negligible when compared to the wall-normal gradient ($\frac{\partial\theta}{\partial x_2}$), the production term can be written as:

$$P_{2\theta} = -v_2'v_2'\frac{\partial\theta}{\partial x_2}, \tag{6.4}$$

where subscripts '1' and '2' denote the streamwise and wall-normal directions respectively. This equation shows the importance of wall-normal fluctuations ($v_n'v_n'$) in the generation of turbulent heat flux. Clearly, from the stress plots in the previous section, it can be seen that the wall-normal stress component decreases from station i_1 to i_2 (see

Figure 6.6 and 6.8). This gets reflected in the thermal flux plots at the two stations. The local flow is laminar here as there is no significant turbulent mixing in the boundary layer at these stations.

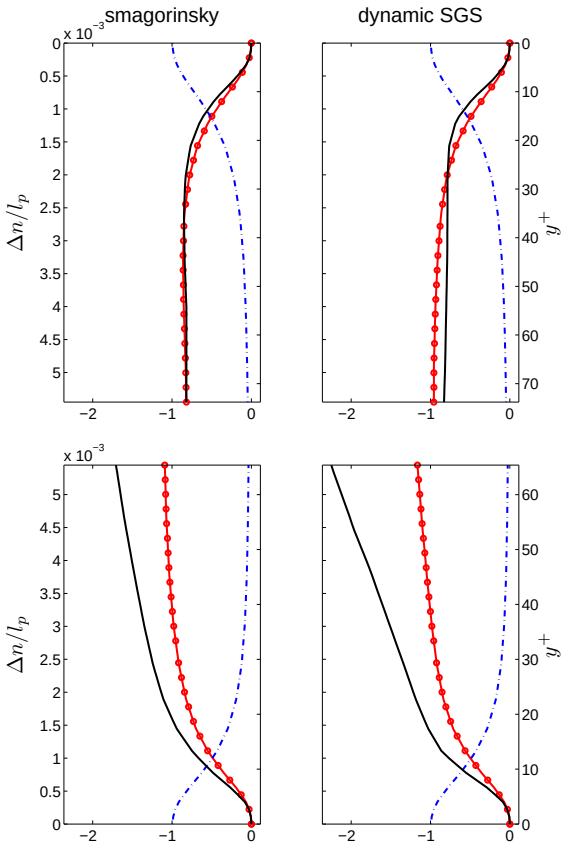

Figure 6.24: Fluxes at i_5; top: pressure side ($x/c_x = 0.976$), bottom: suction side ($x/c_x = 0.973$). Legends: same as in Figure 6.20.

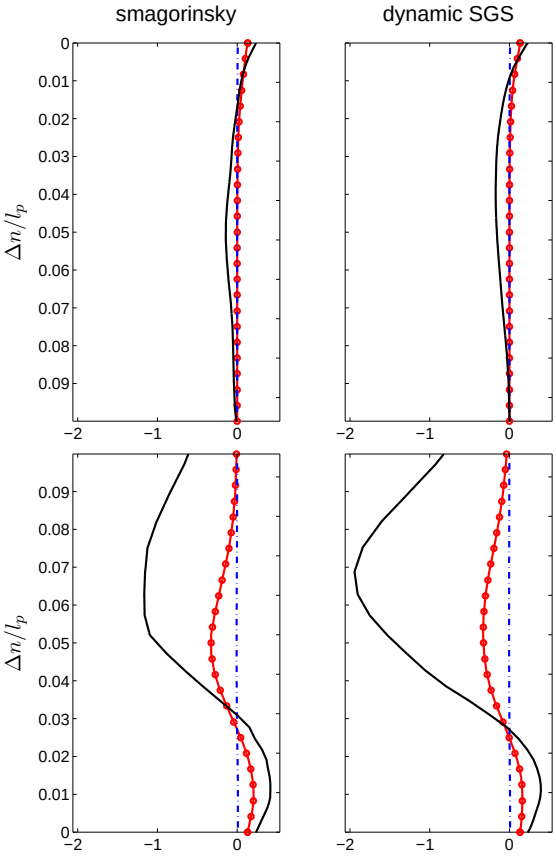

Figure 6.25: Fluxes at i_7; top: pressure side ($x/c_x = 1.711$), bottom: suction side ($x/c_x = 1.711$). Legends: —$\langle -v_x' v_y' \rangle / \tau_w$; -○-$\langle v_y' \theta' \rangle / q_w$; -·-$\left(\frac{\nu}{Pr} \frac{\partial \langle \theta \rangle}{\partial y} \right) / q_w$.

Station i_3 corresponds to the point where the boundary layer is about to get completely turbulent according to the experimental observations. In the simulations, at this station the turbulent heat flux and the shear stress are higher as compared to that at the previous stations. Both the increments are more prominent on the suction side. This proves a higher turbulent mixing of momentum and heat at this station than at the previous ones and this is evident from the elevated Nu profile on the suction side at this station (Figure 6.2). At station i_4 (Figure 6.23), the magnitude of the turbulent (thermal) flux increases further, more prominently on the suction side and the effect can be felt farther away from the surface. This shows that the boundary layer is getting thicker

downstream. The stress plots at this station (see Figure 6.12) also show an increase in wall-normal and shear stress components from the earlier stations – again prominent on the suction side. Station i_5 (Figure 6.24) corresponds to the point close to the trailing edge, and the fluxes are similar to those at i_4. On the pressure side, both the momentum and thermal fluxes are identical, and that probably is due to the streamwise pressure gradient being low on this side.

Figure 6.25 corresponds to the second station in the wake (i_7). The flux components plotted here correspond to the global coordinates as was in case of plotting stresses in the previous section. The local wall shear stress used for normalization is taken as the average of the corresponding values at the last cells of the trailing edge from both suction and pressure sides. The Δn in y-axis is the distance from the corresponding domain boundaries. Merging of the two shear layers from both pressure and suction side is evident from the two distinct peaks of different amplitudes in each of the flux terms (from pressure and suction side).

6.4.3 Turbulent kinetic energy and *rms* fields

In this section the maximum of turbulent kinetic energy (TKE) and *rms* fields over the surface is studied. Along with the TKE (k_t), the normal velocity field (v) corresponding to the global coordinates and the temperature field (θ) are studied. The aim is to study the evolution of the fluctuating fields over the walls. This was motivated by the fact that in 'bypass transition', these fluctuations grow appreciably while going from laminar to turbulent phase. Plots from both smagorinsky and dynamic model are demonstrated.

Figure 6.26, displays the maximum of TKE (k_t) over the cascade surfaces. It also depicts the distance from the surface, scaled by the pitch length (l_p), where the peak value is attained. As per the experiments, the transition zone lies between $x/c_x = 0.32$ and $x/c_x = 0.56$ on the pressure side and between $x/c_x = 0.36$ and $x/c_x = 0.53$ on the suction side (see Figure 6.2). On the pressure side, in both dynamic-SGS and smagorinsky case, there is a slight increase in TKE just before the (experimentally) measured trigger point, but then it decays slowly further downstream. Similarly, on the suction side, at about $x/c_x = 0.33$ the peak in TKE starts to get bigger until around $x/c_x = 0.5$, after which it drops steadily. It can also be seen that these peak fluctuations occur in the boundary layer. It can be concluded that on the suction side, the fluctuations grow in amplitude inside the boundary layer; but they cannot be sustained. These can be associated to the appearance of streaks in the boundary layer. It was discussed earlier that it is important for the free-stream turbulence to keep interacting with the boundary layer in order to force a 'bypass' transition. It might be that in the present case, the streaks are formed but unable to sustain due to the absence of forcing by FST. On the pressure side, on the other hand, no such phenomenon is observed.

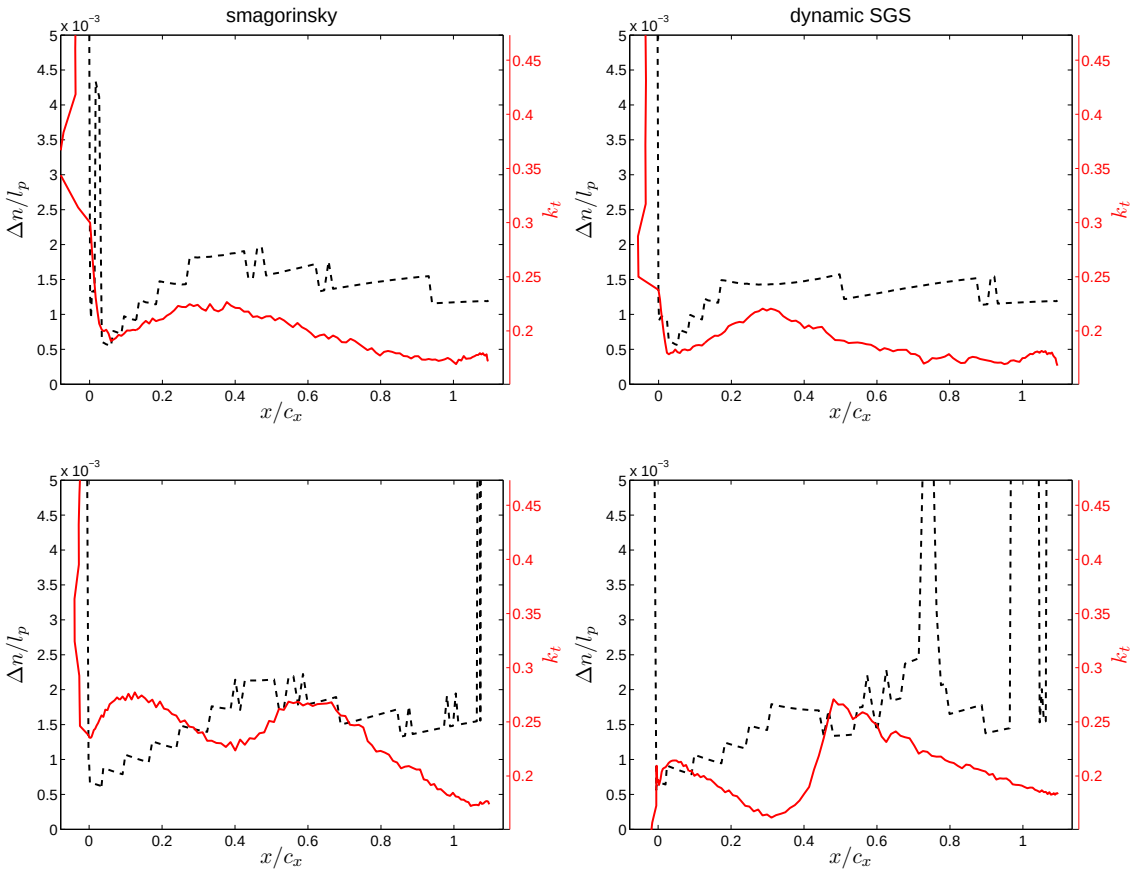

Figure 6.26: Peak TKE (k_t) over the surface; top: pressure side, bottom: suction side. Legends: —$k_t\ |_{max}$ (right y axis); – –distance from wall (left y axis).

Figure 6.27, depicts the maximum of normal fluctuations (v') over the cascade surfaces and the distance from wall where it occurs. It should be noted that the 'v' fluctuation in the global coordinate system is different from wall-normal velocity fluctuations (corresponding the local coordinate system at the wall). Ideally, it is the wall-normal fluctuations that should have been studied. Due to the cumbersomeness of performing coordinate transformation over all the grid points on the walls, and given the fact that after passing the initial 'throat' section of the cascade, the flow is almost parallel (local coordinate system getting close to the global), it was decided to plot the fluctuation component in the global coordinates.

From the plots on the pressure side, it can be observed that the predicted peak fluctuations in the experimentally observed transition zone occur inside the boundary layer. On the other hand, on the suction side, they occur way outside the boundary layer in the free-stream. Downstream of this transition zone (experimentally observed) though, the

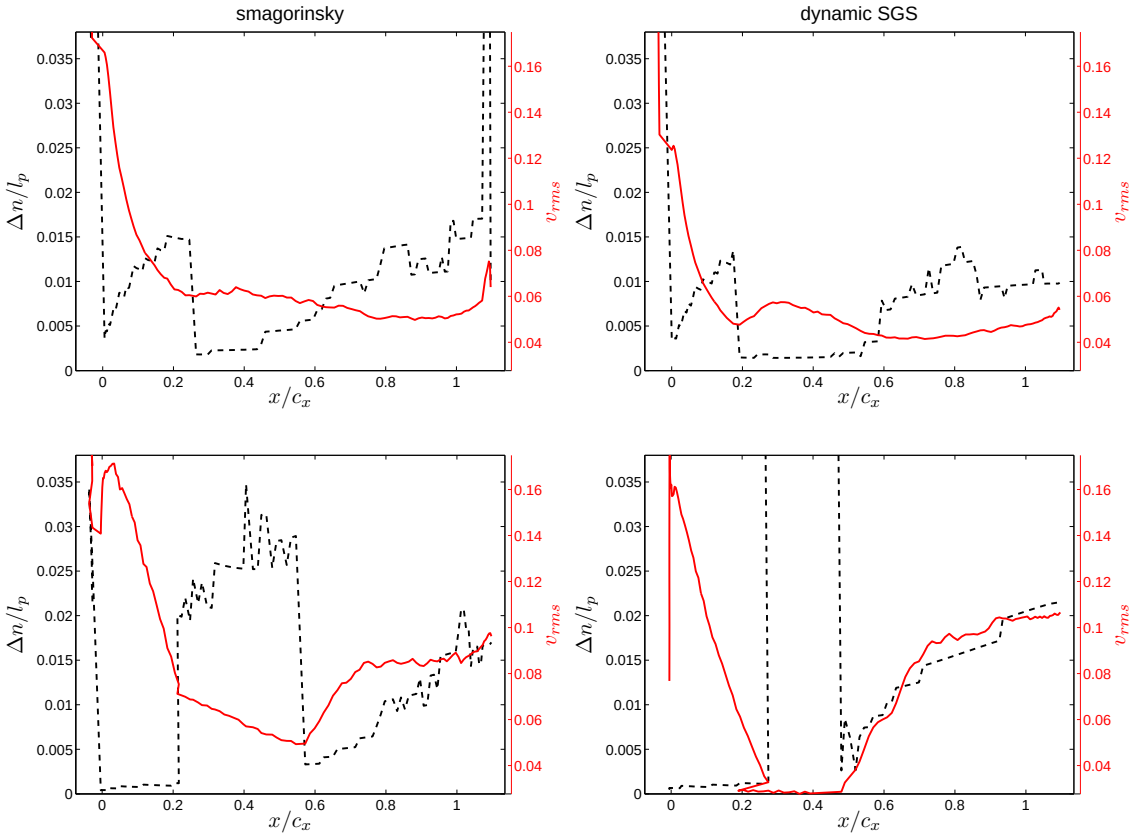

Figure 6.27: Peak v_{rms} over the surface; top: pressure side, bottom: suction side. Legends: —$v_{rms}\ |_{max}$ (right y axis); – –distance from wall (left y axis).

peak moves to almost the edge of the boundary layer or in the free-stream. The magnitude of the peak decreases on the pressure side and it increases on the suction side. It can be said that the normal fluctuations v' on the pressure side, both generated inside the boundary layer and the ones present in the free-stream, are very low. On the suction side, the v' fluctuations in the free-stream are somewhat significant (corresponding to the convected v' from the inlet) but the ones (v' fluctuations) generated in the boundary layer are diminutive. The lack of such fluctuations in the boundary layer shows that there is no real transition in the boundary layer.

The maximum of the temperature fluctuations is also plotted over the cascade surfaces (figure 6.28). It follows a similar trend as the TKE. On the pressure side, the peak fluctuations in the experimentally observed transition zone, occur inside the boundary layer, and the maximum value keeps on increasing downstream gradually. The corresponding distance from the wall keeps decreasing though. On the suction side, a sudden

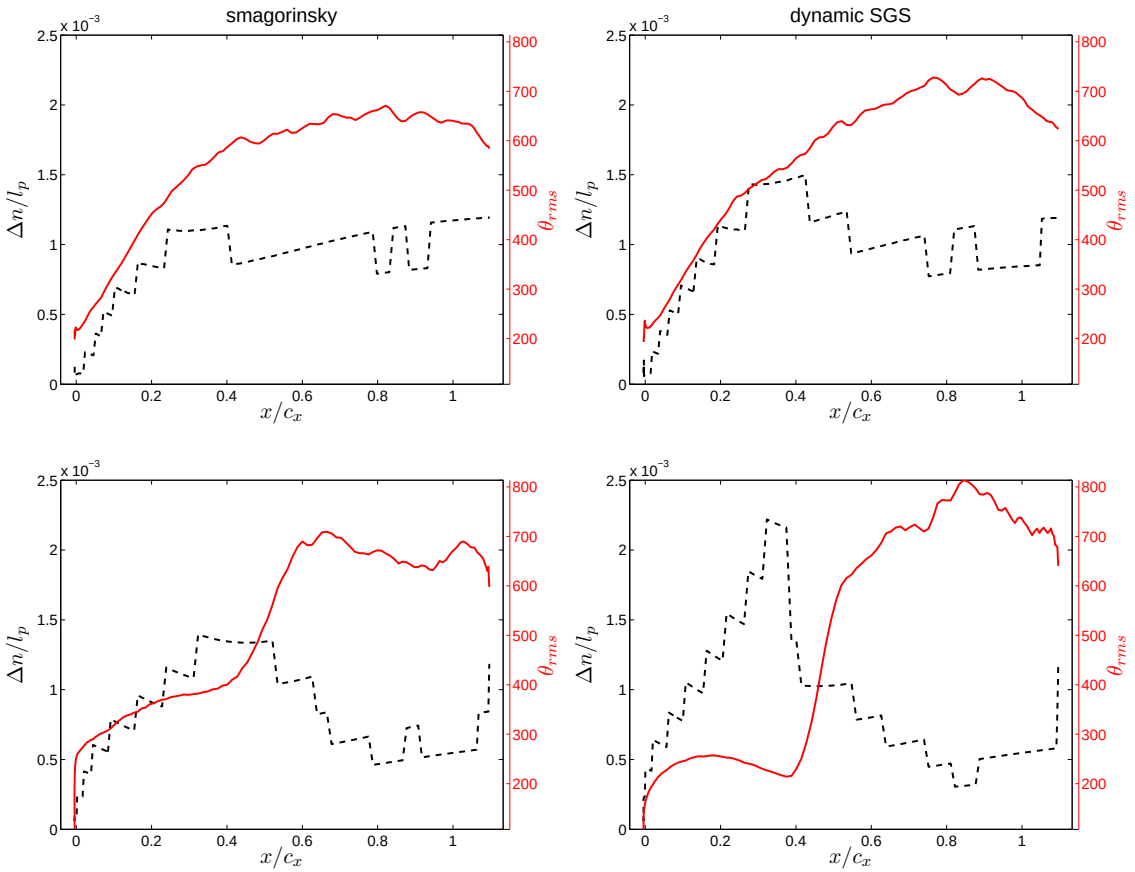

Figure 6.28: Peak θ_{rms} over the surface; top: pressure side, bottom: suction side. Legends: —$\theta_{rms}\mid_{max}$ (right y axis); – –distance from wall (left y axis).

jump is observed around $x/c_x = 0.4$ (experimentally observed onset of transition), and that is observed very close to the wall inside the boundary layer. This is similar to the $k_t \mid max$ curve (figure 6.26). Further downstream, the maximum fluctuation level remains almost constant, but it occurs further close to the boundary.

7

Conclusions and scope for Future Work

7.1 Conclusions

It is observed, finally, that the simulations carried out in the present work are not able to justify the experimental findings. The pressure coefficient (C_p) profile from the simulations showed good agreement with the experiments, but the Nusselt number (Nu) profile did not. The non-linear mechanisms inside the boundary layer responsible for transition seem to never get triggered in the simulations.

A closer look inside the boundary layer showed a gradual but large increment in the streamwise fluctuations on both the sides, as evident from the large increase in the streamwise component of resolved stress. This increment, more prominent on the suction side, also gets reflected in the appreciable increase in Nu just downstream of the experimentally reported transition location. However, the other components, namely, the spanwise and wall-normal components of resolved normal stress, do not show any significant increment. It is expected that the increase in the streamwise component gets redistributed via pressure-strain into the other components – a non-linear mechanism and sign of attaining turbulence. Such a phenomenon is only observed near the trailing edge, which is probably triggered by the unsteadiness of flow downstream of it in the wake region. The reason for the absence of this energy redistribution, on rest of the surface is not clear. Probably, the growth in streamwise fluctuations is not enough to force production in the other directions.

Inspection of the heat flux and shear stress in the boundary layer gives an idea about the penetration of the heat flux in the wall-normal direction due to fluctuations in that direction. The turbulent heat flux along with the Reynolds shear do not show any sub-

stantial rise in the boundary layer in the experimentally observed transition zone. The slight rise in the heat transfer showed by the Nu profile on the suction side can be explained by a similar rise in the thermal flux.

Studying the peak of TKE (k_t) showed that the fluctuations grow appreciably near the experimentally observed transition point, at least on the suction side. It can also indicate a growth of streamwise streaks. But this growth is not sustained, which proves the absence of non-linear interactions triggering transition. It shows probably the need of continuous forcing provided by the FST for these fluctuations to be maintained. More about it can be understood by the nature of FST turbulence outside the boundary layer in this region. The plot showing peak rms value of the normal component of velocity, v, on the other hand, was found to be inconclusive.

A mesh independence study showed that the spanwise resolution or domain size in the spanwise direction had no effect on the transition prediction. A mesh with a finer resolution just in the experimentally observed transition region showed signs of transition. The Nu profile followed the experimental data only about halfway through the transition zone. Then it fails to sustain the growth. Two possibilities are concluded: one, it is merely the effect of numerical error arising out of the uneven mesh, and second, there is a need for very fine streamwise resolution throughout the surface to make the continuous interaction of non-linear modes.

7.2 Scope for future work

In the literature, the concept of 'shear sheltering' is introduced. The sheltering of high frequency disturbances from the free-stream by the wall shear layer is explained. One possibility in the present simulations is that the low frequency fluctuations are not present in the boundary layer. It would be interesting to see how the turbulence evolves from the inflow boundary till it reaches the leading edge, and how the low frequency modes be allowed to enter the boundary layer. Another possibility is that the continuous forcing provided by the FST (high frequency components) is also absent in the present simulations. It is therefore very important to study the evolution of turbulence from inflow boundary to the leading edge. It depends upon many factors like discretization schemes and SGS models.

It would also be interesting to change the resolution in the streamwise direction. A simulation with a mesh refined only in the transition region, showed a small spike locally. But, then again it dropped to the initial levels and continued downstream.

It will be interesting to first study a simple geometry like a flat plate. First, study the receptivity of FST generated by the synthetic isotropic turbulence generation method employed here, and then move on to a more complex geometry like a guide-vane.

Appendices

A

Script for mesh-generation

```
!######################
!## NUMBER OF FACES ##
!######################
41   =i1  !face corresponding i-first
113   =j
1    =k

129  =i2

41   =i3

i1 i2 + 1 -  =i12     !face corresponding i -last
i12 i3 + 1 - =i123

!######################
!## NUMBER OF BLOCKS ##
!######################
DEFMSH
  3
  i1 j k
  i2 j k
  i3 j k

!###################
!#### BLOCK 1 #####
!###################
CURV2
```

```
  1  1 1 1 1 i1
  1
  -2.7289594e-01  -1.5330251e-01    0.    0.009
  1
  -1.0036084e-03  -2.6517036e-02    0.    2e-05
  0

CURV4
  1  i1 1 1 3 j
  2
  2  305  90  0.3  5e-6
  1
  -1.0036084e-03   2.1348296e-01   0.  2  30  90  0.2  5e-6
  4

CURV2
  1  i1 j 1 2 i1
  2
  2e-05
  1
  -2.7289594e-01   8.6697485e-02   0.   0.009
  0

CURV2
  1 1 j 1 4 j
  2
  5e-07
  1
  -2.7289594e-01  -1.5330251e-01   0.   5e-07
  2

!###################
!#### BLOCK 2 #####
!###################
COPYC
  1 i1 1 1 3 j
  2 1 1 1 3 j

CURV1
  2 1 1 1 1 i2
  240
  -1.0036084e-03  -2.6517036e-02   0.0000000e+00
   .
```

```
   .
   .
   .
   (coordinates of the suction-side curve)
   .
   .
   .
   .
   2.6662408e-01   6.0002772e-04   0.0000000e+00
  1 240 2e-04 5e-04 0

CURV4
  2  i2 1 1 3 j
  2
  2  2  90  0.3  5e-07
  1
  2.6662408e-01   2.4060003e-01   0.  2  358  90  0.3  5e-07
  4

CURV1
  2 i2 j 1 2 i2
  225
   2.6662408e-01   2.4060003e-01   0.0000000e+00
   .
   .
   .
   .
   (coordinates of the pressure-side curve)
   .
   .
   .
   .
  -1.0036084e-03   2.1348296e-01   0.0000000e+00
  1 225 5e-04 2e-04 0

!###################
!#### BLOCK 3 #####
!###################
COPYC
  2 i2 1 1 3 j
  3 1  1 1 3 j

CURV2
```

```
  3  1 1 1 1 i3
  2
  2e-04
  1
  6.6495158e-01  -3.5940326e-02   0.          0.009
  0

CURV2
  3 i3 1 1 3 j
  2
  5e-06
  1
  6.6495158e-01   2.0405967e-01   0.          5e-06
  2

CURV2
  3 i3 j 1 2 i3
  2
  0.009
  1
  2.6662408e-01   2.4060003e-01     0.        2e-04
  0

!#########################
!## FILLING THE VOLUME ##
!#########################
FILLB
  1  1 1 1 1 3 i1 j

FILLB
  2  1 1 1 1 3 i2 j

FILLB
  3  i3 1 1 2 3 i3 j

!#########################
!## SMOOTHING OPERATION ##
!#########################
GSMTHB
3
1  1  1  1  1 3  i1 j
2  1  1  1  1 3  i2 j
3  1  1  1  1 3  i3 j
```

```
2
1  i1 1  1  3 1  j
2  1  1  1  3 1  j
0
2  i2 1  1  3 1  j
3  1  1  1  3 1  j
0
0
15

!##################
!## SAVE BLOCKS ##
!##################
TDSR
STORE
1  1 i1  1 j  1 k
block1.bin

TDSR
STORE
2  1 i2  1 j  1 k
block2.bin

TDSR
STORE
3  1 i3  1 j  1 k
block3.bin

!########################
!## MERGING OF BLOCKS ##
!########################
i123 =nni
j    =nnj
k    =nnk

DEFMSH
1
nni nnj nnk

TDSR
RETRIEVE
1  1 i1  1 j  1 k
block1.bin
```

```
TDSR
RETRIEVE
1  i1 i12  1 j  1 k
block2.bin

TDSR
RETRIEVE
1  i12 i123  1 j 1 k
block3.bin

TDSR
STORE
1  1 nni 1 nnj 1 nnk
meshv5.bin

!################
!## SAVE MESH ##
!################
SAVE
volsol.bin
RITFILE
STOP
```

B

Mesh resolution in wall-units

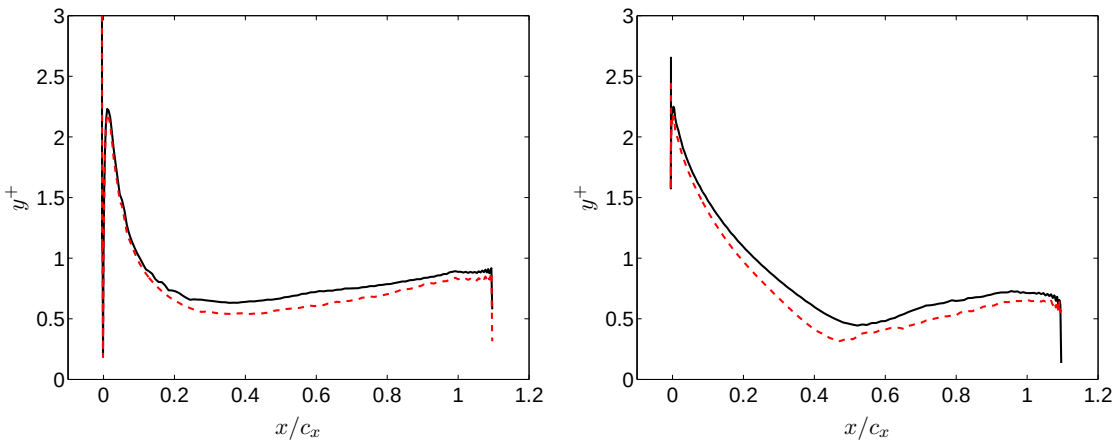

(a) pressure side **(b)** suction side

Figure B.1: Wall y^+ values. LEGENDS: - - Dynamic-SGS; — Smagorinsky. X-coordinates are scaled by the axial-chord length.

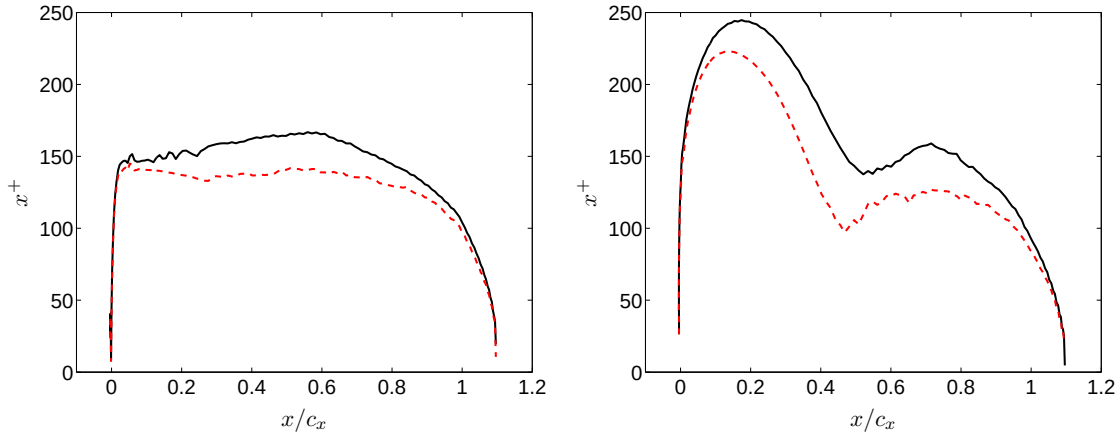

(a) pressure side **(b)** suction side

Figure B.2: Wall x^+ values. LEGENDS: as in Figure B.1.

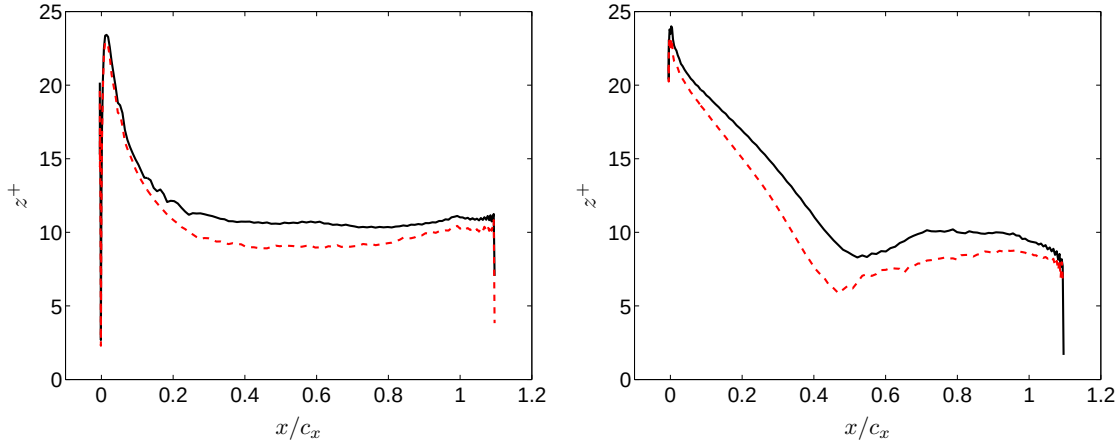

(a) pressure side **(b)** suction side

Figure B.3: Wall z^+ values. LEGENDS: as in Figure B.1.

Bibliography

[1] M. G. Dunn, "Convective heat transfer and aerodynamics in axial flow turbines", Journal of Turbomachinery-Transactions of the ASME 123 (2001) 637–686.

[2] J. C. Han, S. Dutta, S. Ekkad, "Gas Turbine Heat Transfer and Cooling Technology", Second Edition, CRC Press, 2012.

[3] G. Medic, J. Joo, S. Lele, O. Sharma, "Prediction of heat transfer in a turbine cascade with high levels of free-stream turbulence", in: Proceedings of the Summer Program, 2012, p. 147.

[4] E. Collado Morata, N. Gourdain, F. Duchaine, L. Gicquel, "Effects of free-stream turbulence on high pressure turbine blade heat transfer predicted by structured and unstructured LES", International Journal of Heat and Mass Transfer 55 (21) (2012) 5754–5768.

[5] R. Bhaskaran, S. K. Lele, "Large eddy simulation of free-stream turbulence effects on heat transfer to a high-pressure turbine cascade", Journal of Turbulence (11).

[6] J. Hjärne, "Turbine outlet guidvane flows", Ph.D. thesis, Chalmers University of Technology, Göteborg, Sweden (2007).

[7] C. Wang, L. Wang, B. Sundén, V. Chernoray, H. Abrahamsson, "An experimental study of heat transfer on an outlet guide vane", in: ASME Turbo Expo 2014: Turbine Technical Conference and Exposition, American Society of Mechanical Engineers, 2014, pp. V05BT14A001–V05BT14A001.

[8] J. Deschamps-Francoeur, "CFD Study of Heat Transfer Simulations on a Low Pressure Turbine Outlet Guide Vane for On and Off-Design Conditions", Tech. rep., GKN Aerospace Sweden AB (2013).

[9] A. Savill, "One-point closures applied to transition", in: Turbulence and transition modelling, Springer, 1996, pp. 233–268.

[10] L. Cutrone, P. De Palma, G. Pascazio, M. Napolitano, "An evaluation of bypass transition models for turbomachinery flows", International journal of heat and fluid flow 28 (1) (2007) 161–177.

[11] P. R. Voke, Z. Yang, "Numerical study of bypass transition", Physics of Fluids 7 (9) (1995) 2256–2264.

[12] H. Schlichting, K. Gersten, "Boundary-layer theory", Eighth Edition, Springer, 2000.

[13] W. S. Saric, H. L. Reed, E. J. Kerschen, "Boundary-layer receptivity to freestream disturbances", Annual Review of Fluid Mechanics 34 (1) (2002) 291–319.

[14] Y. S. Kachanov, "Physical mechanisms of laminar-boundary-layer transition", Annual Review of Fluid Mechanics 26 (1) (1994) 411–482.

[15] P. Alfredsson, M. Matsubara, "Streaky structures in transition", Transitional boundary layers in aeronautics 46 (1996) 373–386.

[16] P. J. Schmid, "Nonmodal stability theory", Annu. Rev. Fluid Mech. 39 (2007) 129–162.

[17] P. Klebanof, "Effect of free-stream turbulence on a laminar boundary layer", in: Bulletin of the American Physical Society, Vol. 16, 1971, p. 1323.

[18] J. Kendall, "Experimental study of disturbances produced in a pre-transitional laminar boundary layer by weak freestream turbulence", in: AIAA, 18th Fluid Dynamics and Plasmadynamics and Lasers Conference, Vol. 1, 1985.

[19] P. Roach, D. Brierley, "The influence of a turbulent free stream on zero pressure gradient transitional boundary layer development, Part 1:Test cases T3A and T3B", in: Numerical Simulation of Unsteady Flows and Transition to Turbulence, ERCOFTAC Workshop, Cambridge University Press, 1990, pp. 319–347.

[20] K. M. Butler, B. F. Farrell, "Three-dimensional optimal perturbations in viscous shear flow', Physics of Fluids A: Fluid Dynamics (1989-1993) 4 (8) (1992) 1637–1650.

[21] S. Grossmann, "The onset of shear flow turbulence", Reviews of modern physics 72 (2) (2000) 603.

[22] P. Andersson, M. Berggren, D. S. Henningson, "Optimal disturbances and bypass transition in boundary layers", Physics of Fluids (1994-present) 11 (1) (1999) 134–150.

[23] P. Luchini, "Reynolds-number-independent instability of the boundary layer over a flat surface: optimal perturbations", Journal of Fluid Mechanics 404 (2000) 289–309.

[24] M. Matsubara, P. Alfredsson, "Disturbance growth in boundary layers subjected to free-stream turbulence", Journal of Fluid Mechanics 30 (2001) 149–168.

[25] R. G. Jacobs, P. A. Durbin, "Simulations of bypass transition", Journal of Fluid Mechanics 428 (2001) 185–212.

[26] C. E. Grosch, H. Salwen, "The continuous spectrum of the Orr-Sommerfeld equation. Part 1. The spectrum and the eigenfunctions", Journal of Fluid Mechanics 87 (01) (1978) 33–54.

[27] R. G. Jacobs, P. A. Durbin, "Shear sheltering and the continuous spectrum of the Orr–Sommerfeld equation", Physics of Fluids (1994-present) 10 (8) (1998) 2006–2011.

[28] L. Brandt, P. Schlatter, D. S. Henningson, "Transition in boundary layers subject to free-stream turbulence", Journal of Fluid Mechanics 517 (2004) 167–198.

[29] P. Jonáš, O. Mazur, V. Uruba, "On the receptivity of the bypass transition to the length scale of the outer stream turbulence", European Journal of Mechanics-B/Fluids 19 (5) (2000) 707–722.

[30] S. Berlin, D. Henningson, "A nonlinear mechanism for receptivity of free-stream disturbances", Physics of Fluids (1994-present) 11 (12) (1999) 3749–3760.

[31] T. A. Zaki, P. A. Durbin, "Mode interaction and the bypass route to transition", Journal of Fluid Mechanics 531 (2005) 85–111.

[32] M. E. Goldstein, D. W. Wundrow, "On the environmental realizability of algebraically growing disturbances and their relation to Klebanoff modes", Theoretical and computational fluid dynamics 10 (1-4) (1998) 171–186.

[33] S. Nagarajan, S. Lele, J. Ferziger, "Leading-edge effects in bypass transition", Journal of Fluid Mechanics 572 (2007) 471–504.

[34] T. A. Zaki, P. A. Durbin, "Continuous mode transition and the effects of pressure gradient", Journal of Fluid Mechanics 563 (2006) 357–388.

[35] V. Ovchinnikov, M. M. Choudhari, U. Piomelli, "Numerical simulations of boundary-layer bypass transition due to high-amplitude free-stream turbulence", Journal of Fluid Mechanics 613 (2008) 135–169.

[36] X. Wu, P. Moin, "Direct numerical simulation of turbulence in a nominally zero-pressure-gradient flat-plate boundary layer", Journal of Fluid Mechanics 630 (2009) 5–41.

[37] S. Cherubini, P. De Palma, J.-C. Robinet, A. Bottaro, "A purely nonlinear route to transition approaching the edge of chaos in a boundary layer", Fluid Dynamics Research 44 (3) (2012) 031404.

[38] S. Cherubini, J. C. Robinet, P. De Palma, "Numerical study of the effect of freestream turbulence on by-pass transition in a boundary layer", Energy Procedia 45 (2014) 578–587.

[39] H.-J. Kaltenbach, H. Choi, "Large-eddy simulation of flow around an airfoil on a structured mesh", in: Annual Research Briefs 1995, Center for Turbulence Research, Stanford Univ./NASA Ames Research Center, 1995.

[40] S. B. Pope, "Turbulent Flows", First Edition, Cambridge University Press, 2000.

[41] M. Germano, U. Piomelli, P. Moin, W. H. Cabot, "A dynamic subgridscale eddy viscosity model", Physics of Fluids A: Fluid Dynamics 3 (1991) 1760–1765.

[42] D. K. Lilly, "A proposed modification of the germano subgridscale closure method", Physics of Fluids A: Fluid Dynamics 4 (1992) 633.

[43] U. Piomelli, W. H. Cabot, P. Moin, S. Lee, "Subgrid-scale backscatter in turbulent and transitional flows", Physics of Fluids A 3 (7) (1991) 1766–1771.

[44] S. G. Chumakov, "Subgrid models for large eddy simulation: Scalar flux, scalar dissipation and energy dissipation", Ph.D. thesis, University of Wisconsin-Madison (2005).

[45] L. Davidson, S. H. Peng, "Hybrid LES-RANS modelling: a one-equation SGS model combined with a k-ω model for predicting recirculating flows", International Journal for Numerical Methods in Fluids 43 (9) (2003) 1003–1018.

[46] P. Johansson, "A three-dimensional laminar multigrid method applied to the SIMPLEC algorithm", Master's thesis, Dept. of Thermo and Fluid Dynamics, Chalmers University of Technology, Göteborg (1992).

[47] H. K. Versteeg, W. Malalasekera, "An introduction to computational fluid dynamics: the finite volume method", Pearson Education, 2007.

[48] L. Davidson, "Using isotropic synthetic fluctuations as inlet boundary conditions for unsteady simulations", Advances and Applications in Fluid Mechanics 1 (2007) 1–35.

[49] V. Ovchinnikov, U. Piomelli, M. M. Choudhari, "Inflow conditions for numerical simulations of bypass transition", AIAA Paper 2004 0591 (2004) 1–14.

[50] P. Emvin, L. Davidson, "Development and implementation of a fast implicit multigrid method for large eddy simulations", institution, Dept. of Thermo and Fluid Dynamics, Chalmers University of Technology, Göteborg (1997).

[51] L. Davidson, "Fluid mechanics, turbulent flow and turbulence modeling", Lecture Notes, Div. of Fluid Dynamics, Dept. of Applied Mechanics, Chalmers University of Technology, Göteborg (2014).